Fluid modelling of CO_2 dissociation in a dielectric barrier discharge

S. Ponduri[1], M. M. Becker[2], S. Welzel[1,3], M. C. M. van de Sanden[1,3], D. Loffhagen[2], and R. Engeln[1]

[1]Eindhoven University of Technology, P.O. Box 513, 5600 MB Eindhoven, The Netherlands

[2]Leibniz Institute for Plasma Science and Technology, Felix-Hausdorff-Str. 2, 17489 Greifswald, Germany

[3]Dutch Institute for Fundamental Energy Research (DIFFER), P.O. Box 1207, 3430 BE Nieuwegein, The Netherlands

Abstract

The dissociation of CO_2 in a geometrically symmetric dielectric barrier discharge has been analysed by means of numerical modelling. A time- and space-dependent fluid model has been used taking into account the spatial variation of the plasma between the plane-parallel dielectrics covering the electrodes. Main features of the model including an extensive reaction kinetics for the vibrational states of CO_2 are given. The modelling studies have been performed for different applied voltages, discharge frequencies, pressures, gas temperatures and relative permittivities of the dielectrics. The model calculations show that the discharges in the positive and negative half-cycles are different for the considered standard condition leading to a spatially asymmetric distribution of the stable neutrals like CO molecules and O atoms. The generation of CO mainly takes place during the discharge pulses and it is dominated by electron impact dissociation. The specific energy input obtained for the broad range of parameters considered and determined for residence times reported in the literature agrees well with the corresponding experimental values. In accordance with these experiments, the calculated degree of CO_2 conversion has been found to increase almost linearly with the specific energy input. Remaining discrepancies between measured and calculated energy efficiencies are discussed.

1 Introduction

Electricity from renewable energy can be directly used to make synthetic fuels sustainable if electrical discharges could be used to generate CO from CO_2 in an energy efficient manner [1,2]. Research done in the 1970s and 1980s established that non-equilibrium plasmas, i.e., certain kinds of electrical discharges, are capable of dissociating CO_2 with very high energy efficiencies of up to 90 % [3–6] albeit at low throughputs. The advantage of non-equilibrium plasma is that it possesses high electron temperature and vibrational temperature, which promote dissociation reactions, even endothermic reactions, while simultaneously it has a low gas temperature, which prevents backward recombination reactions [6]. In this context, many different non-equilibrium plasma routes have been tested to see if high energy efficiencies can be reproduced. For example, in recent years there were reports

on using a micro-plasma reactor [7], low-pressure RF discharges [8], a gliding arc plasmatron at atmospheric pressure [9] and an atmospheric pressure microwave plasma/catalyst system [10] among others for CO_2 dissociation. In addition, dielectric barrier discharges (DBD) in CO_2 have become subject of recent works [11–19] because their simplicity in operation and potential for scalability offer immense promise for producing CO in industrial scales.

In order to understand the mechanisms of dissociation and to support the prediction of optimal operational parameters, numerical simulations are very important. Quite different modelling approaches are employed for the theoretical investigation of gas discharge plasmas including fluid models, methods that involve a fully kinetic treatment of the charge carriers and so-called hybrid methods [20]. The modelling of discharges in CO_2 has generally been done by means of global reaction kinetic models for the analysis of the dissociation mechanisms. In these models, the corresponding set of rate equations for the different species has been solved to analyse e.g. low-pressure rf discharges [21], dc glow discharges [22] and microwave discharges at moderate pressures [16, 23] in pure CO_2. In addition, various global modelling studies were done for CO_2 laser discharge plasmas [24–31] in different mixtures and dc He-CO_2 glow discharges [7]. In these modelling studies, a more or less extended reaction kinetics was used, where the vibrational relaxation processes of CO_2 were generally not considered.

However, the number of reported works on modelling of the CO_2 dissociation in DBD is rather limited. It has been subject of only a few former works [32] and has started receiving attention only recently again [16, 17, 33, 34]. In these recent works, a zero-dimensional fluid model has been used including an extensive reaction kinetics which takes the vibrational kinetics of CO_2 into account. In contrast, the study reported in [32] used a time-dependent, spatially two-dimensional model solving the continuity equation for the charged particles and Poisson's equation to compute the local electric field, where a simplified set of reactions was taken into account.

Among the various experimental results reported in the literature, the operational parameter space varies significantly and is mainly determined by the reactor size and power source used. To harmonize these results with each other and also with modelling results, two macroscopic parameters, namely the conversion degree

$$\alpha = \frac{n_{\mathrm{CO}}}{n_{\mathrm{CO_2}}} \tag{1}$$

and the specific energy input

$$\mathrm{SEI} = \frac{P}{\Phi} = \frac{P\,t_{\mathrm{r}}}{V}\,, \tag{2}$$

are commonly used to quantify the CO_2 dissociation in a DBD [6, 15]. The conversion degree (1) is given by the ratio of the particle density n_{CO} of CO produced in a certain period of time and the density $n_{\mathrm{CO_2}}$ of CO_2. The specific energy input (2) is defined as the ratio of power P absorbed by the discharge and the gas flow rate Φ which can be related to the residence time t_{r} of a CO_2 molecule in the active plasma volume V according to $t_{\mathrm{r}} = V/\Phi$ [15]. The specific energy input is frequently used in plasma processing [35] and is a measure of the energy density of the plasma. From the quantities α and SEI, the efficiency of CO production η can be calculated according to [15]

$$\eta = \alpha\,\frac{\Delta H_{\mathrm{CO_2}}}{\mathrm{SEI}}\,, \tag{3}$$

where $\Delta H_{\mathrm{CO_2}}$ specifies the dissociation enthalpy of CO_2.

Using a flow reactor, Brehmer *et al.* [15] have recently established that the CO production from CO_2 dissociation in terms of α increases monotonically with the SEI. They also showed that the specific energy input can be considered as the universal scaling parameter for CO_2 conversion to

CO. That is, no matter how a given SEI is attained, i.e. using any combination of applied voltage, flow condition, frequency and dielectric thickness, the production of CO from CO_2 dissociation remains almost constant for that specific energy input [15]. Very similar experimental results about the CO production were reported in [17].

The present paper deals with numerical modelling related to the DBD reactor used in [15] and aims to analyse and explain in more detail the discharge behaviour and the observed trends for similar experimental conditions. A time-dependent, spatially one-dimensional fluid model taking into account an extended vibrational kinetics of CO_2 is employed. Main features of the fluid model and the reaction kinetics used are represented. The fluid model is applied to characterize the spatiotemporal behaviour of discharges taking place in the DBD arrangement under consideration with special focus on the electrical discharge characteristics and the mechanisms of the CO_2 dissociation. In addition, modelling results for a large range of operational parameters are utilized to analyse the CO_2 conversion and energy efficiency and their relation to the specific energy input.

2 Description of the model

The modelling studies presented in this paper are related to the geometrically symmetric DBD built in a flow reactor configuration used in [15]. A schematic representation of this plasma reactor is shown in figure 1a. It consists of a tube that directs the gas flow into the gap between two planar electrodes which form the active zone. The active zone of the DBD is seamlessly connected with another tube which is used to pump out the gas that has been processed between the dielectrics. The reactor configuration is optimized for different experimental diagnostics as e.g. measurement of the CO produced. Several flow tube reactors with thicknesses Δ of the dielectric barriers between 1 and 2 mm and a constant gap width d of 1 mm were used in the experiments. Further details are given in [15].

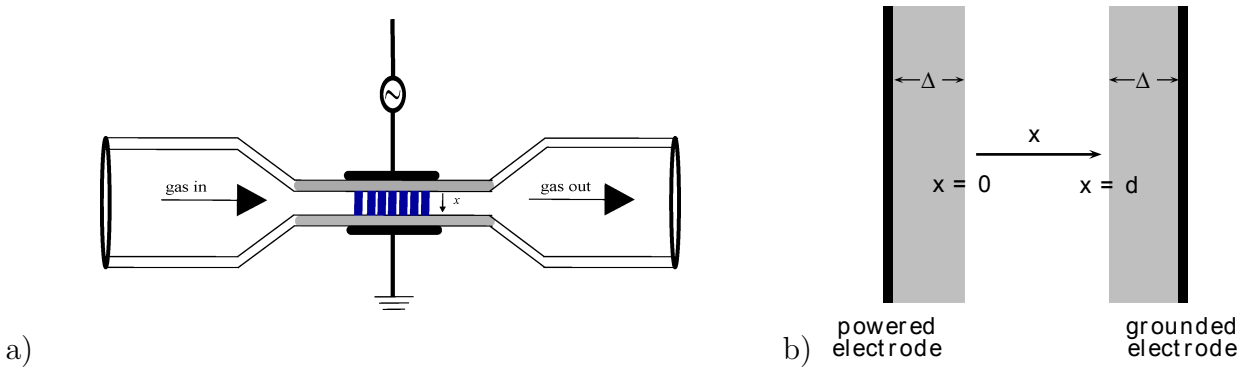

Figure 1: Schematic of the flow reactor geometry used in [15] (a) and the spatially one-dimensional discharge geometry (b) with gap width d and thickness of dielectric layers Δ.

A typical DBD is generally composed of many filaments that are distributed stochastically across the surface of the dielectrics. Thus, a spatially two- or even three-dimensional model including a stochastic description of the filament generation is needed to theoretically describe discharges in this flow reactor configuration. As a step towards such complex modelling, here a time-dependent, spatially one-dimensional approach has been used to model and analyse the spatiotemporal discharge dynamics of the active zone. The corresponding discharge geometry considering the axial component x of the plasma between the plane-parallel, dielectric covered electrodes is displayed in

figure 1b. Such spatially one-dimensional treatment is well suited for the analysis of DBD operating in the homogeneous or glow mode [6] and has successfully been applied for the analysis of single microdischarges e.g. in [36, 37]. Here, the one dimensional description is justified by the fact that the time scales inherent in the discharge plasma are much shorter than the residence time of a unit gas volume in the active plasma zone for the flow rates considered in [15].

2.1 Basic relations

For the theoretical description and anylysis of the symmetric DBD in CO_2 under consideration, a time-dependent, spatially one-dimensional fluid model, based on the one reported in [36], was adapted. The fluid model consists of particle balance equations for the densities n_j of electrons ($j = \mathrm{e}$) and several neutral and charged heavy particles, the electron energy balance equation to determine the mean energy U_e of the electrons and Poisson's equation providing the electric potential ϕ and electric field $E(x,t) = -\partial\phi(x,t)/\partial x$. It is represented by the relations

$$\frac{\partial}{\partial t} n_j(x,t) + \frac{\partial}{\partial x}\Gamma_j(x,t) = S_j(x,t)\,, \tag{4}$$

$$\frac{\partial}{\partial t}\left(n_\mathrm{e}(x,t)U_\mathrm{e}(x,t)\right) + \frac{\partial}{\partial x}Q_\mathrm{e}(x,t) = -e_0\Gamma_\mathrm{e}(x,t)E(x,t) + P_\mathrm{e}(x,t)\,, \tag{5}$$

$$-\frac{\partial^2}{\partial x^2}\phi(x,t) = \frac{e_0}{\varepsilon_0}\sum_j Z_j n_j(x,t)\,, \tag{6}$$

where e_0, ε_0 and Z_j denote the elementary charge, vacuum permittivity and particle charge number, respectively. The particle fluxes Γ_j in (4) and the electron energy flux Q_e in (5) in the x-direction are expressed by the drift-diffusion approximation according to

$$\Gamma_j(x,t) = \mathrm{sgn}(Z_j)b_j(x,t)n_j(x,t)E(x,t) - \frac{\partial}{\partial x}\left(D_j(x,t)n_j(x,t)\right)\,, \tag{7}$$

$$Q_\mathrm{e}(x,t) = -\tilde{b}_\mathrm{e}(x,t)n_\mathrm{e}(x,t)E(x,t) - \frac{\partial}{\partial x}\left(\tilde{D}_\mathrm{e}(x,t)n_\mathrm{e}(x,t)\right)\,. \tag{8}$$

Here, b_j and D_j are the mobility and diffusion coefficient of species j, $\tilde{b}_\mathrm{e}$ and $\tilde{D}_\mathrm{e}$ designate the mobility and diffusion coefficient of electron energy transport and the function $\mathrm{sgn}(Z_j)$ yields the sign of Z_j. Furthermore, the term S_j on the right-hand side of (4) describes the gain and loss of particles in the plasma due to collisional and radiative processes and the terms $-e_0\Gamma_\mathrm{e}E$ and P_e in (5) denote the power input from the electric field and the gain and loss of electron energy resulting from the various collision processes, respectively. The collisional power gain is caused by superelastic electron collisions as well as collisional and associative detachment processes. The collisional power loss considered is due to elastic collisions, electron impact excitation, dissociation, ionization and detachment, electron attachment and electron-ion recombination. A detailed description of these terms can be found e.g. in [38, 39]. In particular, the power gain rate resulting form collisional and associative detachment P^cd is given by

$$P^\mathrm{cd}(x,t) = \sum_p n_p^{(1)}(x,t)n_p^{(2)}(x,t)k_pU_p \tag{9}$$

with the rate coefficient k_p and power gain U_p by an individual detachment process p. Furthermore, the power loss rates due to elastic collisions P^el, inelastic collisions P^in leading to excitation, dissociation, ionization and detachment as well as two-body electron attachment P^at are determined

according to

$$P^{\mathrm{el}}(x,t) = n_{\mathrm{e}}(x,t) \sum_j n_j(x,t) K_j^{\mathrm{el}} \,, \tag{10}$$

$$P^{\mathrm{in}}(x,t) = n_{\mathrm{e}}(x,t) \sum_j n_j(x,t) \sum_m U_{j,m}^{\mathrm{in}} k_{j,m}^{\mathrm{in}} \,, \tag{11}$$

$$P^{\mathrm{at}}(x,t) = n_{\mathrm{e}}(x,t) \sum_j n_j(x,t) K_j^{\mathrm{at}} \,, \tag{12}$$

where the rate coefficient K_j^{el} for energy dissipation in elastic collisions with species j of mass m_j, the rate coefficient $k_{j,m}^{\mathrm{in}}$ of the mth inelastic collision processes of electrons with neutral species j and the individual energy rate coefficients K_j^{at} for two-body electron attachment are given by

$$K_j^{\mathrm{el}} = 2\frac{m_{\mathrm{e}}}{m_j}\sqrt{\frac{2}{m_{\mathrm{e}}}} \int_0^\infty U^2 Q_j^{\mathrm{d}}(U) \left(f_0(U) + k_{\mathrm{B}} T_{\mathrm{g}} \frac{\mathrm{d}}{\mathrm{d}U} f_0(U) \right) \mathrm{d}U \,, \tag{13}$$

$$k_{j,m}^{\mathrm{in}} = \sqrt{\frac{2}{m_{\mathrm{e}}}} \int_0^\infty U Q_{j,m}^{\mathrm{in}}(U) f_0(U) \mathrm{d}U \,, \tag{14}$$

$$K_j^{\mathrm{at}} = \sqrt{\frac{2}{m_{\mathrm{e}}}} \int_0^\infty U^2 Q_j^{\mathrm{at}}(U) f_0(U) \mathrm{d}U \,. \tag{15}$$

These rate coefficients are determined by an integration of the product of electron collision cross section and isotropic part $f_0(U)$ of the electron velocity distribution function (EVDF) over the kinetic energy U of the electrons, where Q_j^{d}, $Q_{j,m}^{\mathrm{in}}$, and Q_j^{at} are the cross section for momentum transfer in elastic collisions, for the inelastic collision process considered with the energy loss $U_{j,m}^{\mathrm{in}}$ and for electron attachment, respectively, k_{B} and T_{g} denote the Boltzmann constant and gas temperature, and $f_0(U)$ is normalized according to $\int_0^\infty \sqrt{U} f_0(U) \mathrm{d}U = 1$.

2.2 Reaction kinetics model

In addition to the electron component, the reaction kinetics model includes the 42 heavy particle species listed in table 1. As products of dissociation reactions of CO_2, carbon monoxide (CO), molecular oxygen (O_2), ozone (O_3) and atomic oxygen (O) are taken into account (species 2–5 in table 1). Because up to 97 % of electron energy can be injected into vibrational excitation in molecular plasmas [5], vibrationally excited states in CO_2 plasmas are particularly important as they are expected to enhance the dissociation rates [6]. Thus, 28 vibrationally exited species (species 6–33 in table 1) are considered to describe the evolution of electron energy accurately and to analyse their role in the CO_2 dissociation. The corresponding statistical weights of the undegenerated vibrational states in the symmetry-stretching (e.g. $CO_2(v_{2a})$) and the asymmetric-stretching ($CO_2(v_{3i})$ with $i = 1, \ldots, 20$) modes are 1 and those of the nth doubly degenerated state $CO_2(0\,n\,0)$ in the bending mode are $n + 1$ [40]. For the mixed vibrational levels $CO_2(v_j)$ with $j = 4, \ldots, 7$ the statistical weights for the individual states were added and $CO_2(v_8)$ is assumed to be in a pure bending mode with 31 quanta so that its statistical weight is 32. Furthermore, two electronically excited states of CO_2, assigned by $^3\Sigma_u^+$ and $^1\Sigma_u^+$, as well as the positive ion of CO_2 in its ground state ($X^2\Pi_g$) and in the two excited states $A^2\Pi_u$ and $B^2\Sigma_u^+$ are taken into consideration. The excited ionic states are introduced to allow for comparison with optional measurements of their optical emission. In addition, the four negative ions O^-, O_2^-, CO_3^- and CO_4^- are included in the reaction kinetics model.

Table 1: List of heavy particle species considered. For excited species and positive ions the excitation/ionization energy threshold is listed, for negative ions the electron affinity is given in the last column.

Number	Species	State	Statistical weight	Energy [eV]
Neutral species in ground state				
1	$CO_2(v_0)$	(0 0 0)	1	0.0
2	CO	–	1	0.0
3	O_2	–	1	0.0
4	O_3	–	1	0.0
5	O	–	1	0.0
Vibrationally excited species				
6	$CO_2(v_1)$	(0 1 0)	2	0.083
7	$CO_2(v_{2a})$	(1 0 0)	1	0.172
8	$CO_2(v_{2b})$	(0 2 0)	3	0.159
9	$CO_2(v_{31})$	(0 0 1)	1	0.291
10	$CO_2(v_{32})$	(0 0 2)	1	0.579
11	$CO_2(v_4)$	(0 3 0)+(1 1 0)	6	0.252
12	$CO_2(v_5)$	(0 4 0)+(1 2 0)+(2 0 0)	9	0.339
13	$CO_2(v_6)$	(1 3 0)+(2 1 0)+(0 5 0)	12	0.442
14	$CO_2(v_7)$	(1 4 0)+(2 2 0)+(3 0 0)	9	0.505
15	$CO_2(v_8)$	sum of higher states	32	2.5
16–33	$CO_2(v_{33})$–$CO_2(v_{320})$	(0 0 3)–(0 0 20)	1	0.87 – 5.24
Electronically excited species				
34	CO_2^*	$^3\Sigma_u^+$	3	7.0
35	CO_2^{**}	$^1\Sigma_u^+$	1	10.5
Positive ions				
36	CO_2^+	$X^2\Pi_g$	4	13.8
37	$CO_2^+(A)$	$A^2\Pi_u$	4	17.6
38	$CO_2^+(B)$	$B^2\Sigma_u^+$	2	18.1
Negative ions				
39	O^-	–	–	1.46
40	O_2^-	–	–	0.45
41	CO_3^-	–	–	3.5
42	CO_4^-	–	–	

The reaction kinetic scheme takes 56 electron impact collision processes with heavy particles into account. These reactions are given in table 2. In addition to elastic collisions contributing directly to the electron energy balance (5), exciting, de-exciting, ionizing, detaching, attaching and recombining electron collision processes with heavy particles are taken into consideration where the corresponding rate coefficients depend on the mean energy U_e of the electrons. For their determination, the collision cross section data of the respective reference was used. In particular, the collision cross sections for electron impact de-excitation processes are determined by use of the principle of detailed balancing using the statistical weights given in table 1. In addition, four collisional or associative detachment processes are included and listed in table 2, which also contribute to the electron energy balance (5). Notice that the interaction of electrons only with CO_2 is taken into account in the present reaction kinetics scheme. This approach is justified by the low conversion degrees of less than 5 % observed in corresponding experiments [12,15] and leads to a decrease of the number of species to be considered in comparison with other recent studies reported e.g. in [16].

Table 2: Electron impact reactions considered in the model. The rate coefficients of reactions E1–E53 are obtained from the solution of the electron Boltzmann equation as a function of the mean electron energy U_e using the cross section data of the respective reference given. The energy rate coefficient for elastic collisions K_1^{el} and the energy rate coefficients for two-body attachment K_j^{at} with $j = 47$–53 are given in eVm^3s^{-1}. All other rate coefficients k_j^{in} with $j = 2$–53 for inelastic (in) two-body electron collision processes are given in m^3s^{-1}, where electron impact excitation (ex), de-excitation (sc – superelastic collision), dissociation (di), ionization (io), detachment (de) and attachment (at) are distinguished. $T_e = 2U_e/(3k_B)$ is the electron temperature in K, and T_g is the gas temperature in K. †: Analogous to E47 and shifted by threshold energy.

Number	Reaction	Rate coefficient	Reference
Elastic electron collisions			
E1	$CO_2(v_0) + e \longrightarrow CO_2(v_0) + e$	$K_1^{el}(U_e)$	[41]
Electron impact excitation and de-excitation of vibrational levels			
E2, E3	$CO_2(v_0) + e \longleftrightarrow CO_2(v_1) + e$	$k_2^{ex}(U_e)$, $k_3^{sc}(U_e)$	[42]
E4, E5	$CO_2(v_0) + e \longleftrightarrow CO_2(v_{2a}) + e$	$k_4^{ex}(U_e)$, $k_5^{sc}(U_e)$	[42, 43]
E6, E7	$CO_2(v_0) + e \longleftrightarrow CO_2(v_{2b}) + e$	$k_6^{ex}(U_e)$, $k_7^{sc}(U_e)$	[43]
E8, E9	$CO_2(v_0) + e \longleftrightarrow CO_2(v_{31}) + e$	$k_8^{ex}(U_e)$, $k_9^{sc}(U_e)$	[42]
E10, E11	$CO_2(v_0) + e \longleftrightarrow CO_2(v_{32}) + e$	$k_{10}^{ex}(U_e)$, $k_{11}^{sc}(U_e)$	[44]
E12, E13	$CO_2(v_0) + e \longleftrightarrow CO_2(v_4) + e$	$k_{12}^{ex}(U_e)$, $k_{13}^{sc}(U_e)$	[42]
E14, E15	$CO_2(v_0) + e \longleftrightarrow CO_2(v_5) + e$	$k_{14}^{ex}(U_e)$, $k_{15}^{sc}(U_e)$	[42]
E16, E17	$CO_2(v_0) + e \longleftrightarrow CO_2(v_6) + e$	$k_{16}^{ex}(U_e)$, $k_{17}^{sc}(U_e)$	[42]
E18, E19	$CO_2(v_0) + e \longleftrightarrow CO_2(v_7) + e$	$k_{18}^{ex}(U_e)$, $k_{19}^{sc}(U_e)$	[42]
E20, E21	$CO_2(v_0) + e \longleftrightarrow CO_2(v_8) + e$	$k_{20}^{ex}(U_e)$, $k_{21}^{sc}(U_e)$	[42]
E22, E23	$CO_2(v_1) + e \longleftrightarrow CO_2(v_{2b}) + e$	$k_{22}^{ex}(U_e)$, $k_{23}^{sc}(U_e)$	Analogous to E2 [42]
E24, E25	$CO_2(v_1) + e \longleftrightarrow CO_2(v_4) + e$	$k_{24}^{ex}(U_e)$, $k_{25}^{sc}(U_e)$	Analogous to E6 [43]
E26, E27	$CO_2(v_1) + e \longleftrightarrow CO_2(v_5) + e$	$k_{26}^{ex}(U_e)$, $k_{27}^{sc}(U_e)$	Analogous to E12 [42]
E28, E29	$CO_2(v_{2a}) + e \longleftrightarrow CO_2(v_5) + e$	$k_{28}^{ex}(U_e)$, $k_{29}^{sc}(U_e)$	Analogous to E4 [42, 43]
E30, E31	$CO_2(v_{2b}) + e \longleftrightarrow CO_2(v_4) + e$	$k_{30}^{ex}(U_e)$, $k_{31}^{sc}(U_e)$	Analogous to E2 [42]
E32, E33	$CO_2(v_{2b}) + e \longleftrightarrow CO_2(v_5) + e$	$k_{32}^{ex}(U_e)$, $k_{33}^{sc}(U_e)$	Analogous to E4+E6 [42]
E34, E35	$CO_2(v_{31}) + e \longleftrightarrow CO_2(v_{32}) + e$	$k_{34}^{ex}(U_e)$, $k_{35}^{sc}(U_e)$	Analogous to E8 [42]
E36, E37	$CO_2(v_4) + e \longleftrightarrow CO_2(v_5) + e$	$k_{36}^{ex}(U_e)$, $k_{37}^{sc}(U_e)$	Analogous to E2 [42]
Electron impact excitation and de-excitation of electronically excited states			
E38, E39	$CO_2(v_0) + e \longleftrightarrow CO_2^* + e$	$k_{38}^{ex}(U_e)$, $k_{39}^{sc}(U_e)$	[42]
E40, E41	$CO_2(v_0) + e \longleftrightarrow CO_2^{**} + e$	$k_{40}^{ex}(U_e)$, $k_{41}^{sc}(U_e)$	[42]
Electron impact dissociation			
E42	$CO_2(v_0) + e \longrightarrow CO + O + e$	$k_{42}^{di}(U_e)$	[41]
Electron impact ionization and detachment			
E43	$CO_2(v_0) + e \longrightarrow CO_2^+ + e + e$	$k_{43}^{io}(U_e)$	[41]
E44	$CO_2(v_0) + e \longrightarrow CO_2^+(A) + e + e$	$k_{44}^{io}(U_e)$	[41]
E45	$CO_2(v_0) + e \longrightarrow CO_2^+(B) + e + e$	$k_{45}^{io}(U_e)$	[41]
E46	$O^- + e \longrightarrow O + e + e$	$k_{46}^{de}(U_e)$	[45, 46]
Dissociative electron attachment			
E47	$CO_2(v_0) + e \longrightarrow CO + O^-$	$k_{47}^{at}(U_e)$, $K_{47}^{at}(U_e)$	[47]
E48	$CO_2(v_1) + e \longrightarrow CO + O^-$	$k_{48}^{at}(U_e)$, $K_{48}^{at}(U_e)$	[47]†
E49	$CO_2(v_{2a}) + e \longrightarrow CO + O^-$	$k_{49}^{at}(U_e)$, $K_{49}^{at}(U_e)$	[47]†
E50	$CO_2(v_{2b}) + e \longrightarrow CO + O^-$	$k_{50}^{at}(U_e)$, $K_{50}^{at}(U_e)$	[47]†
E51	$CO_2(v_{31}) + e \longrightarrow CO + O^-$	$k_{51}^{at}(U_e)$, $K_{51}^{at}(U_e)$	[47]†
E52	$CO_2(v_4) + e \longrightarrow CO + O^-$	$k_{52}^{at}(U_e)$, $K_{52}^{at}(U_e)$	[47]†
E53	$CO_2(v_5) + e \longrightarrow CO + O^-$	$k_{53}^{at}(U_e)$, $K_{53}^{at}(U_e)$	[47]†
Dissociative electron-ion recombination			
E54	$CO_2^+ + e \longrightarrow CO + O$	$4.2 \times 10^{-13}(T_e/300)^{-0.75}$	[48]
E55	$CO_2^+(A) + e \longrightarrow CO + O$	$4.2 \times 10^{-13}(T_e/300)^{-0.75}$	[48]

E56	$CO_2^+(B) + e \longrightarrow CO + O$	$4.2 \times 10^{-13}(T_e/300)^{-0.75}$	[48]
Collisional and associative detachment			
E57	$O^- + CO_2(v_0) \longrightarrow O + CO_2(v_0) + e$	4.0×10^{-18}	[30]
E58	$O^- + CO \longrightarrow CO_2(v_{2b}) + e$	$5.8 \times 10^{-15}(T_g)^{-0.4}$	[49]
E59	$O^- + O \longrightarrow O_2 + e$	2.3×10^{-16}	[50]
E60	$O_2^- + O \longrightarrow O_3 + e$	1.5×10^{-16}	[29]

In addition to the collision processes involving electrons, further 257 heavy particle collision processes and two radiation processes are considered. In order to allow for an analysis of the vibrational energy transfer, an extended set of reactions describing the vibrational-translational (VT) and vibrational-vibrational (VV) relaxation processes is used. The corresponding reactions and rate coefficients are listed in tables 3 and 4. Furthermore, 16 collisions between neutrals in their ground state, non-detaching ion-neutral reactions such as charge transfer reactions as well as ion-ion recombination processes are taken into account as given in table 5. In this table the two radiation processes (from excited ions) are listed as well.

Table 3: Vibrational-translational relaxation reactions considered in the model. The rate coefficients refer to a gas temperature of 400 K and are given in m^3s^{-1}. †: $j = 3, \ldots, 20$; $c_j = j - 2$.

Number	Reaction	Rate coefficient	Reference
VT1	$CO_2(v_1) + CO_2(v_0) \longrightarrow CO_2(v_0) + CO_2(v_0)$	1.06×10^{-20}	[51]
VT2	$CO_2(v_{2b}) + CO_2(v_0) \longrightarrow CO_2(v_1) + CO_2(v_0)$	2.15×10^{-20}	[51]
VT3	$CO_2(v_{2a}) + CO_2(v_0) \longrightarrow CO_2(v_0) + CO_2(v_0)$	9.68×10^{-20}	[51, 52]
VT4	$CO_2(v_{2a}) + CO_2(v_0) \longrightarrow CO_2(v_{2b}) + CO_2(v_0)$	6.92×10^{-17}	[52]
VT5	$CO_2(v_{31}) + CO_2(v_0) \longrightarrow CO_2(v_0) + CO_2(v_0)$	1.0×10^{-23}	[6]
VT6	$CO_2(v_{31}) + CO_2(v_0) \longrightarrow CO_2(v_1) + CO_2(v_0)$	1.66×10^{-23}	[51]
VT7	$CO_2(v_{31}) + CO_2(v_0) \longrightarrow CO_2(v_4) + CO_2(v_0)$	6.04×10^{-21}	[51]
VT8	$CO_2(v_{32}) + CO_2(v_0) \longrightarrow CO_2(v_{31}) + CO_2(v_0)$	5.0×10^{-23}	[6]
VT9	$CO_2(v_4) + CO_2(v_0) \longrightarrow CO_2(v_{2b}) + CO_2(v_0)$	3.20×10^{-20}	[51]
VT10	$CO_2(v_4) + CO_2(v_0) \longrightarrow CO_2(v_1) + CO_2(v_0)$	8.96×10^{-24}	[51]
VT11	$CO_2(v_5) + CO_2(v_0) \longrightarrow CO_2(v_4) + CO_2(v_0)$	6.46×10^{-20}	[51]
VT12	$CO_2(v_5) + CO_2(v_0) \longrightarrow CO_2(v_{31}) + CO_2(v_0)$	1.72×10^{-22}	[51]
VT13	$CO_2(v_5) + CO_2(v_0) \longrightarrow CO_2(v_{2b}) + CO_2(v_0)$	5.95×10^{-26}	[51]
VT14	$CO_2(v_6) + CO_2(v_0) \longrightarrow CO_2(v_5) + CO_2(v_0)$	9.62×10^{-20}	[51]
VT15	$CO_2(v_6) + CO_2(v_0) \longrightarrow CO_2(v_4) + CO_2(v_0)$	2.65×10^{-23}	[51]
VT16	$CO_2(v_7) + CO_2(v_0) \longrightarrow CO_2(v_6) + CO_2(v_0)$	2.12×10^{-20}	[51]
VT17	$CO_2(v_8) + CO_2(v_0) \longrightarrow CO_2(v_7) + CO_2(v_0)$	3.18×10^{-20}	[51]
VT18–VT35	$CO_2(v_{3j}) + CO_2(v_0) \longrightarrow CO_2(v_{3(j-1)}) + CO_2(v_0)$	$c_j \times 10^{-22}$	[6]†

Table 4: Table of vibrational energy exchange reactions used in the model. The rate coefficients refer to a gas temperature of 400 K and are given in m^3s^{-1}. †: $i = 2, \ldots, 19$; ‡:$j = 2, \ldots, i$; $c_i = 10$ for $i \leq 9$; $c_i = (19 - i)$ for $10 \leq i \leq 15$; $c_i = (20 - i)$ for $16 \leq i \leq 19$.

Number	Reaction	Rate coefficient	Reference
VV1	$CO_2(v_{2b}) + CO_2(v_0) \longrightarrow CO_2(v_1) + CO_2(v_1)$	1.01×10^{-18}	[51]
VV2	$CO_2(v_{31}) + CO_2(v_{31}) \longrightarrow CO_2(v_{32}) + CO_2(v_0)$	1.0×10^{-16}	[6]
VV3	$CO_2(v_4) + CO_2(v_1) \longrightarrow CO_2(v_{2b}) + CO_2(v_{2b})$	2.99×10^{-18}	[51]
VV4	$CO_2(v_4) + CO_2(v_4) \longrightarrow CO_2(v_{2b}) + CO_2(v_5)$	8.30×10^{-17}	[52]

VV5	$CO_2(v_5) + CO_2(v_0) \longrightarrow CO_2(v_4) + CO_2(v_1)$	3.07×10^{-18}	[51]
VV6	$CO_2(v_5) + CO_2(v_1) \longrightarrow CO_2(v_4) + CO_2(v_{2b})$	6.03×10^{-18}	[51]
VV7	$CO_2(v_5) + CO_2(v_{2b}) \longrightarrow CO_2(v_4) + CO_2(v_4)$	9.24×10^{-18}	[51]
VV8	$CO_2(v_5) + CO_2(v_5) \longrightarrow CO_2(v_4) + CO_2(v_6)$	1.30×10^{-15}	[52]
VV9	$CO_2(v_6) + CO_2(v_0) \longrightarrow CO_2(v_5) + CO_2(v_1)$	4.58×10^{-18}	[51]
VV10	$CO_2(v_6) + CO_2(v_1) \longrightarrow CO_2(v_5) + CO_2(v_{2b})$	9.24×10^{-18}	[51]
VV11	$CO_2(v_6) + CO_2(v_{2b}) \longrightarrow CO_2(v_5) + CO_2(v_4)$	1.52×10^{-17}	[51]
VV12	$CO_2(v_6) + CO_2(v_6) \longrightarrow CO_2(v_7) + CO_2(v_5)$	1.30×10^{-15}	[52]
VV13	$CO_2(v_7) + CO_2(v_0) \longrightarrow CO_2(v_6) + CO_2(v_1)$	2.76×10^{-16}	[52]
VV14	$CO_2(v_7) + CO_2(v_1) \longrightarrow CO_2(v_6) + CO_2(v_{2b})$	5.53×10^{-16}	[52]
VV15	$CO_2(v_8) + CO_2(v_0) \longrightarrow CO_2(v_7) + CO_2(v_1)$	1.31×10^{-15}	[52]
VV16–VV33	$CO_2(v_{3i}) + CO_2(v_{31}) \longrightarrow CO_2(v_{3(i+1)}) + CO_2(v_0)$	1.0×10^{-16}	[6]†
VV34–VV204	$CO_2(v_{3i}) + CO_2(v_{3j}) \longrightarrow CO_2(v_{3(i+1)}) + CO_2(v_{3(j-1)})$	$c_i \times 10^{-17}$	[6]†,‡

Table 5: Neutral-neutral, ion-neutral and ion-ion collision processes as well as radiative transition processes used in the model. The rate-coefficients have the units of m^3s^{-1} for two-body collisions, m^6s^{-1} for three-body collisions and s^{-1} for radiative transitions. The gas temperature T_g is given in K.

Number	Reaction	Rate coefficient	Reference
Neutral kinetics of ground state particles			
N1	$CO_2(v_0) + O \longrightarrow CO + O_2$	$2.8 \times 10^{-17} \exp(-26500/T_g)$	[53]
N2	$CO + O_2 \longrightarrow CO_2(v_0) + O$	$4.2 \times 10^{-18} \exp(-24000/T_g)$	[53]
N3	$CO + O + CO_2(v_0) \longrightarrow CO_2(v_0) + CO_2(v_0)$	$1.6 \times 10^{-45} \exp(-1510/T_g)$	[22]
N4	$O_2 + O_3 \longrightarrow O_2 + O_2 + O$	$7.26 \times 10^{-16} \exp(-11400/T_g)$	[50]
N5	$O_2 + O + CO_2(v_0) \longrightarrow O_3 + CO_2(v_0)$	$1.7 \times 10^{-42} T_g^{-1.2}$	[22]
N6	$O_2 + O + O_2 \longrightarrow O_3 + O_2$	$8.61 \times 10^{-43} T_g^{-1.25}$	[54]
N7	$O_2 + O + O \longrightarrow O_3 + O$	$2.15 \times 10^{-40} \exp(345/T_g)$	[50]
N8	$O_3 + O \longrightarrow O_2 + O_2$	$1.81 \times 10^{-17} \exp(-2300/T_g)$	[54]
N9	$O + O + CO_2(v_0) \longrightarrow O_2 + CO_2(v_0)$	$3.81 \times 10^{-42} T_g^{-1.0} \exp(-170/T_g)$	[33]
Ion-atom and ion-molecule reactions (including charge transfer)			
I1	$O^- + CO_2(v_0) + CO_2(v_0) \longrightarrow CO_3^- + CO_2(v_0)$	9.0×10^{-41}	[25]
I2	$O_2^- + CO_2(v_0) + CO_2(v_0) \longrightarrow CO_4^- + CO_2(v_0)$	1.2×10^{-40}	[29]
I3	$O_2^- + O \longrightarrow O_2 + O^-$	1.5×10^{-16}	[29]
I4	$CO_3^- + O \longrightarrow O_2^- + CO_2(v_0)$	1.1×10^{-16}	[29]
I5	$CO_4^- + O \longrightarrow CO_3^- + O_2$	1.4×10^{-16}	[29]
Ion-ion recombination			
I6	$CO_2^+ + CO_3^- \longrightarrow CO_2(v_0) + CO_2(v_0) + O$	5.0×10^{-13}	[25]
I7	$CO_2^+ + CO_4^- \longrightarrow CO_2(v_0) + CO_2(v_0) + O_2$	5.0×10^{-13}	[25]
Radiative transitions			
R1	$CO_2^+(A) \longrightarrow CO_2^+ + h\nu$	6.1×10^6	[55]
R2	$CO_2^+(B) \longrightarrow CO_2^+ + h\nu$	7.2×10^6	[55]

2.3 Transport and electron rate coefficients

In order to describe the flux of particles and electron energy according to (7) and (8), the corresponding transport coefficients are required. The mobility of the positive and negative ions specified in table 1 are determined as a function of the reduced electric field E/N, where N is the number density of the neutral gas. Here, the mobility of CO_2^+ in CO_2 given in [56] and of O^- and CO_3^-

in CO_2 according to [57] are employed. The mobility of O_2^- and CO_4^- is assumed to be the same as that of O^- and CO_3^-, respectively. The corresponding diffusion coefficients are calculated using the Einstein relation [6]. Regarding the neutral species, the diffusion coefficient of CO_2 in CO_2 is taken from the relation $ND_{CO_2} = 3.07 \times 10^{20}\,\mathrm{m^{-1}s^{-1}}$ according to [58], where the same value is also used for all vibrationally and the electronically excited states. Furthermore, the coefficients $ND_{CO} = 9.86 \times 10^{18}\,\mathrm{m^{-1}s^{-1}}$ [59], $ND_{O_2} = 7.3 \times 10^{20}\,\mathrm{m^{-1}s^{-1}}$ [59] and $ND_O = 6.5 \times 10^{18}\,\mathrm{m^{-1}s^{-1}}$ [22] are used and the diffusion coefficient of O_3 in CO_2 is assumed to be the same as that of O_2.

In the framework of the present fluid model, the local-mean-energy approximation is used for the description of the electron properties [60]. That is the transport and rate coefficients of the electrons including the coefficients (13) and (15) are determined in advance from the solution of the steady-state, spatially homogeneous electron Boltzmann equation using the collision cross section data according to table 2. The kinetic equation of the electrons has been solved for given reduced electric field, gas temperature and cross section data in multiterm approximation of the EVDF expansion in Legendre polynomials using a generalized version of the method described in [61] adapted to take nonconservative electron collisions and the random motion of gas particles into account. The resulting coefficients have subsequently been put into look-up tables as a function of the mean electron energy U_e and used in the model calculations. Notice that the consistent coefficients $\tilde{b}_e$ and $\tilde{D}_e$ of the electron energy transport have been utilized instead of the frequently used simplified expressions $\tilde{b}_e = 5U_e b_e/3$ and $\tilde{D}_e = 5U_e D_e/3$ [62].

Based on the solution of the electron Boltzmann equation, it is also possible to get an impression of the fraction of power transferred from plasma electrons to different channels of collisions of the CO_2 molecule. Using equations (13), (14) and (15), the fraction of transferred power can be calculated by dividing the energy rate coefficient $K^{\mathrm{el}}_{CO_2}$ for elastic collisions, the individual energy rate coefficient $U^{\mathrm{in}}_{CO_2,m} k^{\mathrm{in}}_{CO_2,m}$ for the mth inelastic collision process and the energy rate coefficient $K^{\mathrm{at}}_{CO_2}$ for two-body electron attachment, respectively, by the total energy rate coefficient $K^{\mathrm{el}}_{CO_2} + \sum_m U^{\mathrm{in}}_{CO_2,m} k^{\mathrm{in}}_{CO_2,m} + K^{\mathrm{at}}_{CO_2}$. The resulting fractions of power transferred to different channels as a function of the mean electron energy are shown in figure 2.

It is found that almost all power is dissipated in vibrational excitation of CO_2 for mean energies below about 1.2 eV, where the excitation of the asymmetric mode level $CO_2(v_{31})$, i.e., $CO_2(0\,0\,1)$, is generally the dominant one. The contribution of this vibrational excitation decreases for larger mean energies and the electron impact excitation of the electronically excited states $CO_2(^3\Sigma_u^+)$ and $CO_2(^1\Sigma_u^+)$ becomes predominant above about $U_e = 3\,\mathrm{eV}$. The electron impact dissociation of CO_2 ground state molecules consumes 1 % of power transferred at a mean energy of 3.5 eV increasing to about 5 % at larger U_e. The fraction of power dissipated in ionizing collisions increases continuously above about 2.0 eV and becomes larger than the dissociation for $U_e = 3.8\,\mathrm{eV}$. At the same time, the contribution of the momentum transfer in elastic collisions and the dissociative electron attachment are of minor importance in general. These results show great similarity with those presented e.g. in [6, 33], where an analysis with respect to the reduced electric field dependence is represented.

This global consideration indicates that low mean energies (and reduced electric fields) are favourable for CO_2 dissociation that is induced by vibrational up-pumping along the asymmetric mode. Nonetheless, for vibrational up-pumping to contribute significantly to CO_2 dissociation, a remarkable population of vibrational levels is required, which, in turn, leads to modifications of the discussion due to the expected impact of superelastic electron collisions of the distribution function similar to the results for nitrogen reported in e.g. [63].

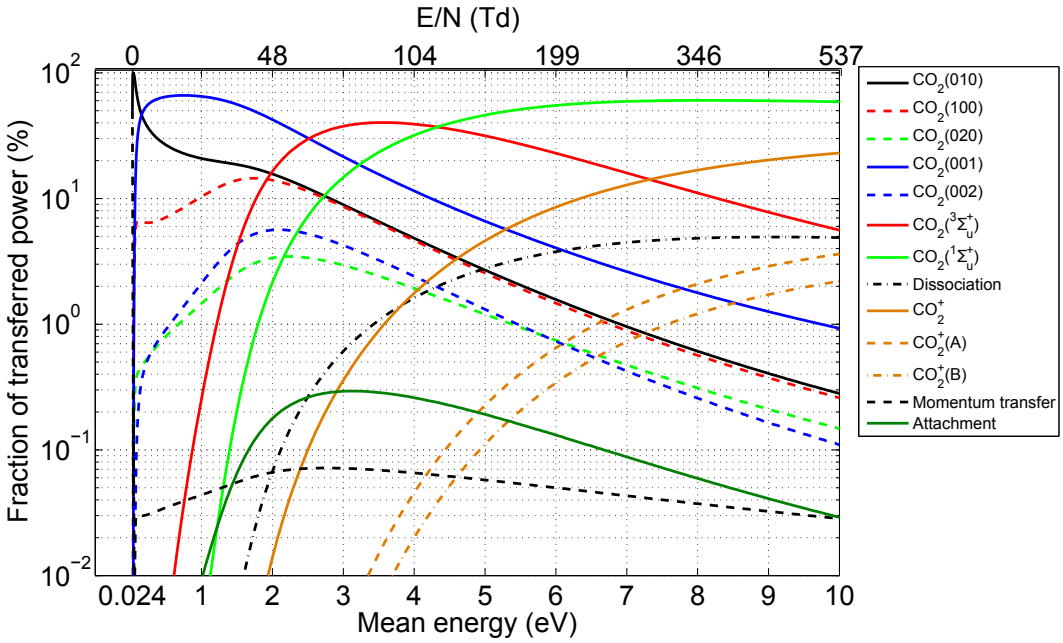

Figure 2: Fraction of power transferred into important channels as a function of mean electron energy at $T_\mathrm{g} = 400\,\mathrm{K}$. Selected reduced electric field values are also added. Only important channels are shown for the sake of clarity.

2.4 Boundary conditions and solution method

The system of partial differential equations (4)–(6) including the fluxes (7) and (8) is completed by appropriate boundary conditions. For the heavy particles, the electrons and the electron energy density, flux boundary conditions are employed at the dielectric surfaces in front of the electrodes at $x = 0$ and $x = d$ (cf. figure 1b) taking into account partial reflection of the particles with reflection coefficients of 0.3 for electrons and neutral species and 0.001 for ions. Additionally, the emission of secondary electrons caused by positive ions impinging onto the surface is considered assuming a secondary electron emission coefficient of 0.02. Further details of these boundary conditions are given in [36].

For the determination of the electric potential and electric field in the gap, a sinusoidal voltage $U_0(t) = V_0 \sin(2\pi f t)$ with amplitude V_0 and frequency f is applied at the powered electrode ($x = -\Delta$) and the potential at the grounded electrode ($x = d + \Delta$) is zero. To describe adequately the accumulation of surface charges on the dielectrics the condition [36, 64]

$$\varepsilon_\mathrm{r}\varepsilon_0 E_\mathrm{diel}(x_0, t) \cdot \nu - \varepsilon_0 E(x_0, t) \cdot \nu = \sigma(x_0, t) \tag{16}$$

is used at the plasma boundaries, where the parameter ν is given by $\nu = -1$ at $x_0 = 0$ and $\nu = 1$ at $x_0 = d$, respectively. The electric field E_diel inside the dielectrics with relative permittivity ε_r is obtained from the assumption of an immediate drop of the space charges inside the dielectrics by the Laplace equation and the temporal variation of the surface charge density σ results from the particle currents impinging onto the dielectrics [36].

The numerical solution of the resulting set of equation has been realized using the finite-difference method according to [36, 65]. In particular, an adaptive time stepping is used for the model calculation performed using 500 non-equidistant intervals with logarithmic meshing for the spatial grid. The calculations were done on Intel® Xeon® processors E5-2603 with a processing speed of 1.8 GHz. A typical calculation of 20 voltage cycles at a discharge frequency of 130 kHz lasted about 5 days.

Parameter	Standard condition	Parameter variation
Frequency [kHz]	130	60, 90
Pressure [mbar]	1000	600, 700, 800, 900
Voltage amplitude [kV]	10.0	8.0, 8.5, 9.0, 9.5, 10.5 11.0
Gas temperature [K]	400	300, 350, 450, 500
Dielectric permittivity	3.8	4.5, 6.0

Table 6: Standard condition and parameter variations used for the model calculations.

3 Results and discussion

In order to analyse the behaviour of the CO_2 DBD in the reactor configuration used in [15] by means of numerical modelling, a number of different operational parameters have been considered. These values are listed in table 6 and were selected on basis of the experimental conditions studied in [15]. The standard condition represents typical discharge parameters and was chosen as a reference to illustrate the main discharge features and the importance of different processes responsible for CO production. Note that the values for the relative permittivity of the dielectrics are a representative of quartz. Beginning with the standard condition, usually one parameter is changed for the respective parameter variation while keeping the other parameters constant. For all conditions, a gap width of $d = 1\,\mathrm{mm}$ and a dielectric thickness of $\Delta = 2\,\mathrm{mm}$ are used.

The model calculations start at the time $t = 0$ from a spatially homogeneous distribution of the particle densities assuming a quasineutral plasma with a particle density of $1.0 \times 10^3\,\mathrm{cm}^{-3}$ for the positive ions and the electron component with an initial mean energy of 2.0 eV and of $5.0 \times 10^2\,\mathrm{cm}^{-3}$ for the negative ions. The spatiotemporal evolution of the DBD has usually been calculated for 20 voltage cycles of the respective frequency, which corresponds to about 0.154 ms at the standard condition. This time is chosen such that there are enough cycles to get good average properties while simultaneously keeping the assumption that electrons mainly interact only with CO_2.

In the following, results for the DBD at standard condition are discussed at first. Then, the results obtained by model calculations for the different operational parameters given in table 6 are analysed with special focus on the conversion degree and energy efficiency and their relation to the specific energy input which can be considered as the universal scaling parameter for CO_2 conversion to CO according to the related experimental work of [15].

3.1 Discharge behaviour at standard condition

The analysis of the behaviour of the DBD at standard condition focuses on the electrical discharge characteristics and the mechanisms of the CO_2 dissociation.

3.1.1 Electrical discharge characteristics

The temporal evolution of the applied voltage, the gap voltage and the discharge current density as well as the spatiotemporal evolution of the electron density, mean electron energy and reduced electric field are shown in figure 3. Because already after few cycles a quasi-periodic state establishes for these properties at the discharge conditions considered, here the three cycles 18 to 20 are shown, where the electrical characteristics are identical in every cycle. Since a sinusoidal voltage signal is

applied to the powered electrode of the DBD, each electrode alternates between being cathode and anode. That is, for half of the period one electrode is the instantaneous cathode (lower voltage compared to the other electrode) and for the next half-period it is the instantaneous anode (higher voltage compared to the other electrode). On the basis of this alternating nature of a DBD, another classification is generally made, where a voltage cycle is divided into positive and negative half-cycle. The positive half-cycle takes place when a positive voltage is applied at the powered electrode, while the negative half-cycle occurs when a negative voltage is applied. These classifications are helpful in simplifying the discussion in the following sections.

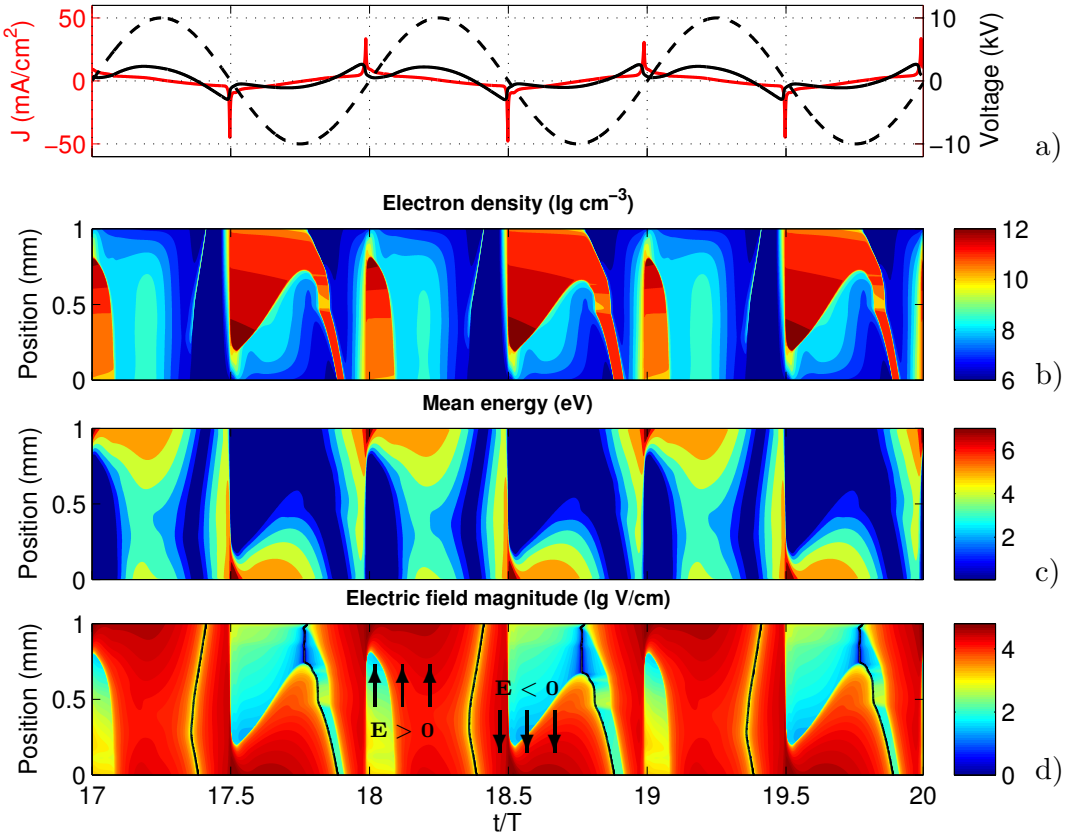

Figure 3: Temporal variation of applied voltage (- - -), gap voltage (—) and discharge current density (a), and spatiotemporal distribution of electron density in logarithmic scale (b), mean electron energy (c) and electric field magnitude (d) for the standard condition given in table 6 with $T = 1/f = 7.69\,\mu$s. The black lines in (d) mark the positions at which the sign (direction) of the electric field changes. The direction of the electric field is also identified.

It can be seen from the characteristics of the voltage and discharge current density displayed in figure 3a that there is one discharge event every half-cycle. Each peak in the discharge current density

$$J(t) = \frac{1}{d}\int_0^d \left[\varepsilon_0 \frac{\partial}{\partial t} E(x,t) + e_0 \sum_i Z_i \Gamma_i(x,t)\right] \mathrm{d}x \tag{17}$$

corresponds to a discharge event which lasts approximately 100–200 ns. The gap voltage

$$V_\mathrm{g}(t) = \phi(0,t) - \phi(d,t) \tag{18}$$

increases until the breakdown voltage of 2.4 kV in positive and 2.7 kV in negative half-periods is reached. In both half-cycles the discharge starts with an ionization wave from the instantaneous

anode which reaches the instantaneous cathode after few nanoseconds. There is an increase in the electron density and mean electron energy (cf. figures 3b and 3c) during ignition of the discharge at a large electric field (figure 3d) and a subsequent decline once the ionization wave approaches to the opposite electrode.

As it can be seen from the figure 3b, the electron density starts to increase at the instantaneous anode and reaches a maximum at a certain distance from the instantaneous cathode during the discharge event. This distance at which the maximum electron density occurs during positive and negative half-cycles is denoted as d_0 and corresponds to the thickness of the cathode fall region. It is approximately 200 μm for the standard condition. After breakdown the electrons drift towards the anode where they are partly absorbed. Note that in negative half-cycles not all electrons reach the anode before the polarity changes. The remaining electrons drift back to the former cathode as it becomes the anode in the following discharge. Figures 3c,d show that the mean electron energy as well as the electric field have their maxima in the cathode-fall region. However, the electron density in front of the cathode is small and thus the highest electron induced CO_2 dissociation is expected to occur in the cathode sheath to plasma transition region. Plasma electrons, i.e. electrons not in the sheath, have a low mean energy of less than 1 eV and thus the CO_2 dissociation in collisions with plasma electrons is of minor importance (cf. figure 2).

As it can be noticed from all the discharge characteristics, there is a difference in positive and negative half-cycles. Discharges occurring in negative half-cycles are characterized by, i.a., a higher breakdown voltage, stronger current peak and longer period with higher electron density compared to discharges in positive half-cycles. This asymmetry is caused by the relatively high frequency of 130 kHz, which does not allow the charge carriers to recombine completely between subsequent discharge events. The resulting volume memory effect leads to a mutual influence of the discharges occurring in positive and negative half-cycles. Golubovskii *et al.* [66] have observed a similar difference between positive and negative half-cycles in a helium discharge. In their model, they attributed this difference to the slow recombination of He_2^+ ions. They could reduce the memory effect and thus the differences between positive and negative half-cycles by using an artificially increased recombination rate coefficient for electron-ion recombination.

In order to understand the influence of the charged particles on the observed asymmetry in the discharge evolution, the spatiotemporal behaviour of the densities of charged particles is plotted in figure 4. Instead of three cycles as in the figure 3, only one representative cycle (18.45–19.45) is chosen to capture the important features of both half-cycles. Obviously, there is a clear difference in the spatiotemporal evolution of the charged particles between positive and negative half-cycles. The density of the CO_2^+ ions shown in figure 4a decays slowly after ignition of discharges in the negative half-cycle due to electron-ion recombination according to processes E54–E56 in table 2. Note that the density of the excited ionic states CO_2^+(A) and CO_2^+(B) amounts only to 10 % of the total positive ion density during the discharge phase and is smaller than 2 % of the total positive ion density in the off-phase. Since the time between subsequent discharges of about 3.7 μs at $f = 130$ kHz is much smaller than the recombination time, which is in the range of milliseconds, the positive ion density decays by less than one order of magnitude until ignition of the following discharge in the positive half-cycle. During the positive half-cycle electron-ion recombination is less important due to the lower density of electrons. Because the magnitude of the electric field between the electrodes is larger during the positive half-cycle compared to the negative half-cycle (cf. figure 3d), a pronounced positive ion drift to the instantaneous cathode ($x = d$) occurs and thus the positive ion density in the gap decreases stronger compared to the negative half-cycle. At $t/T = 19.2$ few new positive ions are generated in front of the instantaneous anode at $x = 0$ because the mean electron energy slightly exceeds the threshold for ionization of CO_2 molecules in electron

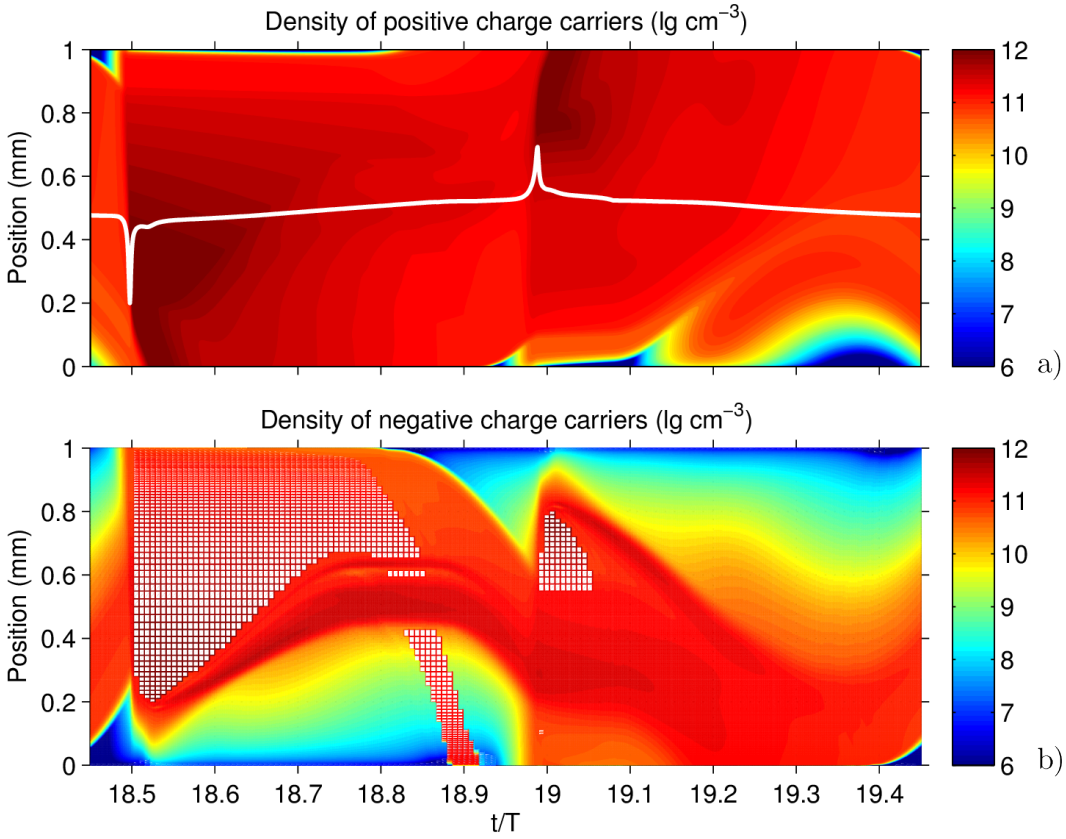

Figure 4: Spatiotemporal behaviour of the density of CO_2^+ ions, including its excited states (a) and density of all negative ions (surface) and electrons (grid lines) (b) in logarithmic scale for the standard condition given in table 6 with $T = 1/f = 7.69\,\mu$s. The white line in (a) marks the discharge current for a better understanding of the temporal position. In (b) the electron density exceeds the density of negative ions in regions where grid lines are shown.

collisions at this position (cf. figure 3c).

Even larger differences between the negative and the positive half-cycle are found in the spatiotemporal evolution of the negative charge carriers shown in figure 4b. In the negative half-cycle electrons are the dominant negatively charged species in the plasma region, whereas negative ions dominate in the cathode-fall region. Here, CO_3^- is the dominant negative ion becauce of its efficient generation from O^- according to reaction I1 in table 5. Its particle density contributes to more than 95 % to the total density of negative ions during the entire period. Due to their larger mass compared to the electron component, negative ions respond more inertly to the change of the electric field direction at $t/T \approx 18.8$ (cf. figure 3d). As a result, most negative ions remain in the gap until re-ignition of the discharge in the positive half-cycle and constitute the dominant negatively charged species here in contrast to the dominance of electrons during the negative half-cycle. Ion-ion recombination according to the processes I6 and I7 in table 5 is the dominant loss channel of negative ions. But it is too slow for a marked reduction of their particle density within one voltage half-cycle. Note that CO_3^- has also been found to be the dominant negative ion in pure CO_2 plasmas at the respective conditions studied by experiments [67] and modelling [33].

3.1.2 Mechanisms of CO_2 dissociation

In order to analyse the mechanisms of CO_2 dissociation generating CO and O, the spatiotemporal distributions of CO and O particle densities are displayed in figure 5 for the standard condition.

Starting from a spatially homogeneous distribution of these species with an initial particle density of

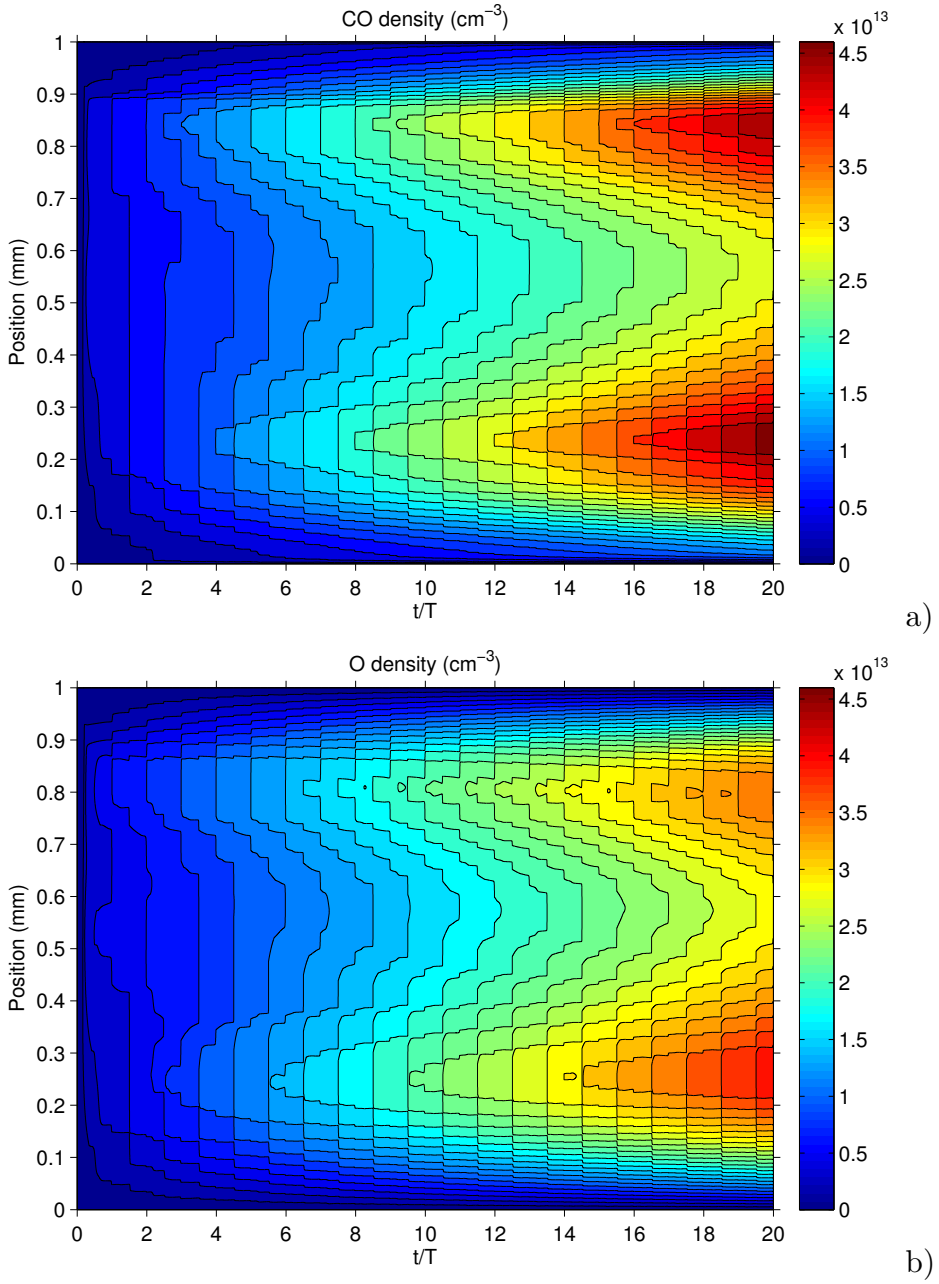

Figure 5: Spatiotemporal behaviour of the particle density of CO (a) and O (b) calculated for the standard condition with $T = 1/f = 7.69\,\mu$s.

$1.0 \times 10^3\,\mathrm{cm}^{-3}$, the densities of CO and O gradually increase in time. Both these species are mainly generated around d_0. The slight asymmetry of their spatial density distribution is a consequence of the differences in the discharge behaviour during the positive and negative half-cycle (cf. figure 3). At the end of the calculation the density of CO is slightly larger than that of O because the dissociative electron attachment to CO_2 according to reaction E47 in table 2 leads to an additional generation of CO, while it does not produce O. Furthermore, the loss processes of CO and O in table 5 due to heavy particle collisions are comparatively inefficient during the period of time considered and the diffusion of both these species takes place with comparable velocity.

To analyse the contribution of the different CO production channels, the rates of CO production

due to electron impact dissociation (reaction E42 in table 2), dissociative electron attachment to CO_2 (reactions E47–E53 in table 2) and dissociative electron-ion recombination (reactions E54–E56 in table 2) are shown in figure 6 together with the temporal variation of the discharge current density and the spatially integrated CO density over one representative voltage cycle (t/T = 18.45–19.45 in figure 3). It is found that the CO density shows a step-like increase during the short discharge

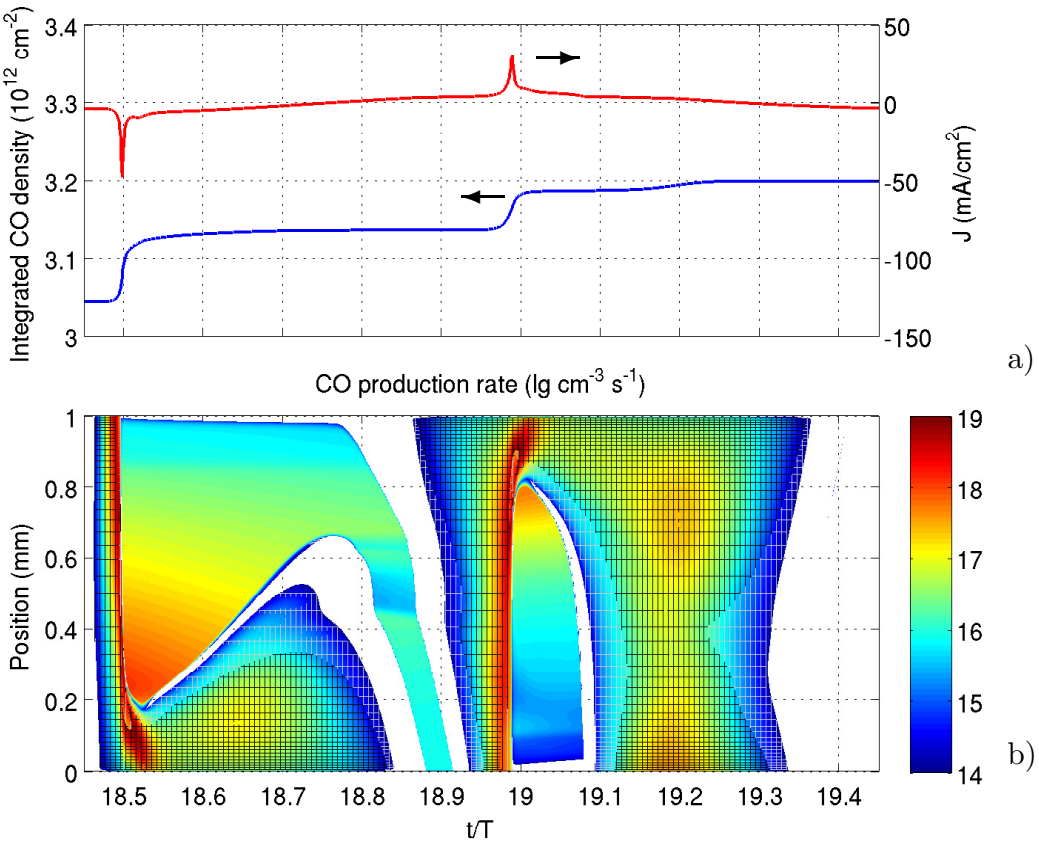

Figure 6: Temporal variation of current density and spatially integrated CO density (a) and spatiotemporal change of the CO production (b) due to electron impact dissociation (black grid lines), dissociative attachment (grey grid lines) and dissociative recombination (surface without grid lines) over one representative voltage cycle. In blank regions the CO production rates are smaller than $1.0 \times 10^{14}\,\mathrm{cm^{-3}s^{-1}}$.

events, while it remains almost constant for the rest of the cycle (figure 6a). The representation of the CO production rates in figure 6b points out that the steep increase during the current pulses results mainly from electron impact dissociation with weaker contributions caused by dissociative electron attachment. Immediately after breakdown, electron-ion recombination weakly contributes to the CO_2 splitting in the plasma region as well. In contrast to the negative half-cycle, a second weaker increase of the CO density occurs in the positive half-cycle at $t/T \approx 19.2$ (cf. figure 6a) because of a further marked increase of the electron impact dissociation rate (cf. figure 6b) in accordance with the spatiotemporal change of the mean energy and particle density of the electrons in figure 3.

A quantification of the different contributions of the electron processes to the CO production can be obtained by considering the period-integrated density production of CO at every position in the gap. The particle density $N_{j,m}(x)$ of a species j generated by the two-body electron collision

process m during the period $T = 1/f$ is given by

$$N_{j,m}(x) = \int_{t_0}^{t_0+T} n_\mathrm{e}(x,t) n_m(x,t) k_{j,m}(U_\mathrm{e}(x,t)) \mathrm{d}t \tag{19}$$

in the framework of the fluid model, where n_m denotes the density of the collision partner in the process m, $k_{j,m}$ is the corresponding collision rate coefficient depending on the mean electron energy (cf. equation (14)) and t_0 denotes a certain instant of the periodic state. The resulting densities of CO generated by electron impact dissociation (reaction E42 in table 2), by dissociative electron attachment to CO_2 (reactions E47–E53), by dissociative electron-ion recombination (reactions E54–E56), respectively and in total during one voltage cycle are shown in figure 7.

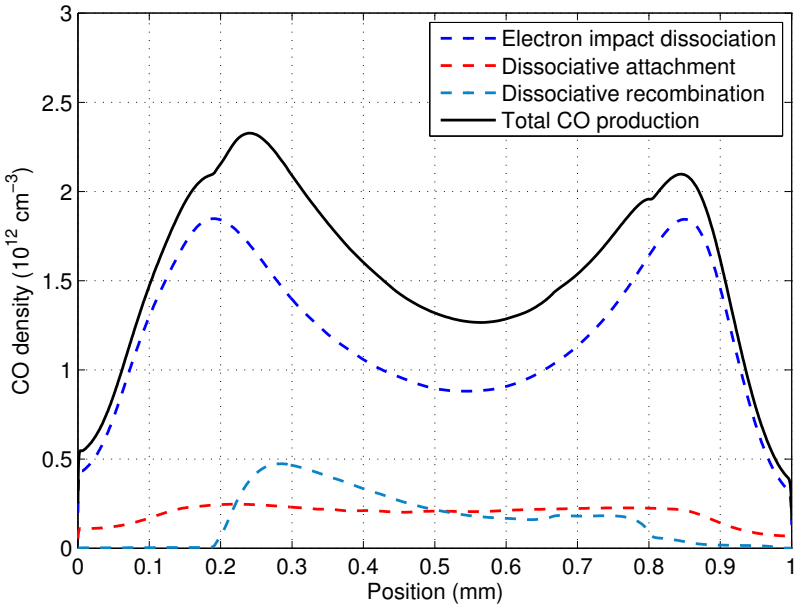

Figure 7: Spatial variation of the CO molecules generated during one voltage cycle by electron impact dissociation, dissociative electron attachment, dissociative electron-ion recombination and in total, respectively, during one voltage cycle.

The results confirm that the CO_2 dissociation in electron collisions is the dominant CO production channel. Furthermore, it becomes obvious that dissociative attachment and recombination processes contribute with almost equal parts of about 10 % to the CO production. Figure 7 also highlights the spatial asymmetry of the CO production which is caused by the differences in negative and positive half-cycles. In particular, it becomes obvious that the asymmetry of the CO density shown in figure 5a is mainly caused by different contributions of electron-ion recombination in positive and negative half-cycles.

Apart from electron collision processes, the collision process between ground state CO_2 and oxygen atoms (reaction N1 in table 5) can lead to a generation of CO in the framework of the present model. However, the corresponding rate coefficient is such small in the gas temperature range considered that its contribution is negligible.

Another reaction chain that can become relevant for the CO_2 dissociation is the vibrational up-pumping along the asymmetric stretch according to the reactions VV2 and VV16–VV204 in table 4. Since the vibrational energy exchange among the levels of the asymmetric mode reaction channel is comparatively fast, it can lead to considerable densities of highly excited states of this

mode, where finally the dissociation energy of CO_2 of 5.5 eV is exceeded and dissociation takes place. Here, the state $CO_2(v_{320})$ is close to the dissociation energy and its density is considered as a representative for CO generated by vibrational up-pumping. In figure 8 the temporal evolution of the spatially averaged particle density of $CO_2(v_{320})$ is illustrated. When comparing this result with the CO density generated by electron impact dissociation, dissociative electron attachment and dissociative electron-ion recombination, it becomes immediately obvious that vibrational up-pumping is negligible for the discharge conditions and period of time considered. This finding is in agreement with the results of zero-dimensional modelling studies of a DBD at atmospheric pressure recently reported in [16], where a similar chain of vibrational up-pumping reactions was considered.

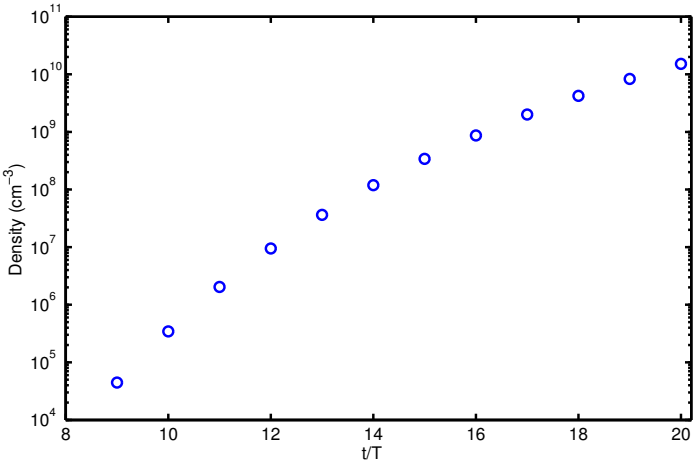

Figure 8: Temporal evolution of the spatially averaged particle density of $CO_2(v_{320})$ generated by vibrational up-pumping at the standard condition.

3.2 Universal scaling parameter of CO_2 dissociation

According to the analysis of the related DBD experiment given in [15], the specific energy input (2) can be considered as the universal scaling parameter for the CO_2 conversion to CO. Because a flow of the gas transverse to the direction of the discharge is not considered in the spatially one-dimensional model and thus the residence time t_r of gas molecules in the active plasma zone is an open parameter, the power spent per CO_2 molecule

$$P_{CO_2} = \frac{P_d}{n_{CO_2}} \tag{20}$$

is introduced and correlated with the CO_2 conversion frequency $\Delta n_{CO}/(n_{CO2}T)$ in figure 9. Here, the average power density P_d is determined by

$$P_d = \frac{f}{d}\int_{t_0}^{t_0+T} J(t)V_g(t)\,dt \tag{21}$$

and Δn_{CO} denotes the increase of the spatially averaged CO density during one voltage cycle of length $T = 1/f$. The results represented in figure 9 have been obtained by a number of model calculations for the operational parameters given in table 6, where only one parameter with respect to the standard condition was changed for the respective parameter variation. Obviously, a linear

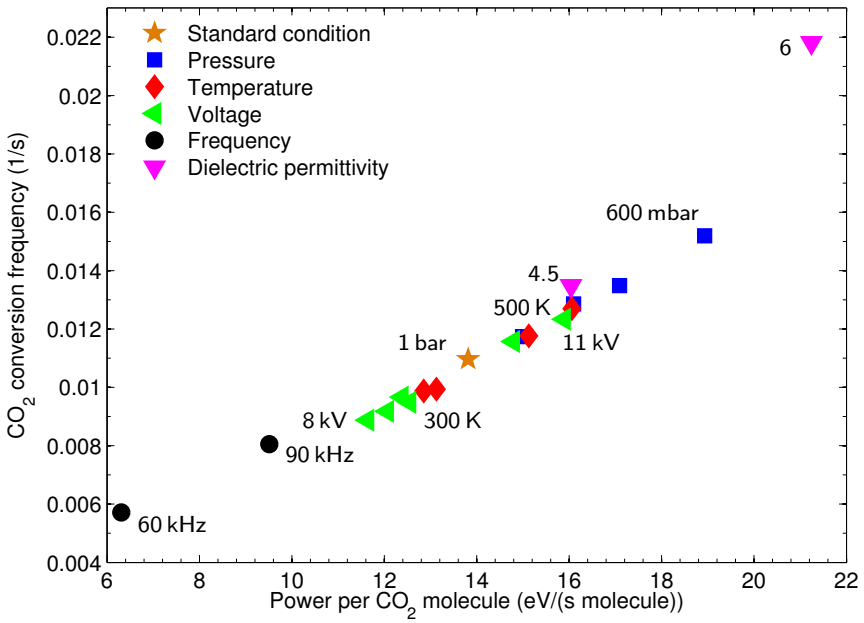

Figure 9: CO_2 conversion frequency as a function of P_{CO_2} for the parameter conditions of table 6.

dependence of the conversion frequency on the power spent per CO_2 molecule is obtained for all discharge conditions considered. In particular, the CO_2 conversion frequency increases linearly with increasing temperature, voltage and frequency, respectively, while the gas pressure has an inverse effect. A decrease of the pressure leads to higher power per CO_2 molecule and at the same time to a higher CO_2 conversion. Furthermore, a markedly higher power density with raised conversion frequency is obtained for dielectrics with a relative permittivity of 6.

The linear dependence of the CO_2 conversion on the power spent per CO_2 molecule predicted by the model calculations for the variation of five parameters is in good agreement with the experimental results reported in [15]. For the range of SEI reported in [15], a similar scaling of the CO_2 conversion has also been observed in [16], where a global time-dependent model was applied for the theoretical description of an atmospheric pressure DBD using a constant average power density and gas temperature as input.

A parameter that allows the direct comparison of the modelling results with experimental data is the energy efficiency of CO production η according to equation (3). It is defined as the ratio of the dissociation enthalpy $\Delta H_{CO_2} = 2.9\,\mathrm{eV}$ [15, 16] of CO_2 and the energy that is consumed to generate one CO molecule. The division of the conversion frequencies represented in figure 9 by the corresponding power values yields values for η in the range between 0.2 and 0.3 %. These values are about one order of magnitude smaller than the efficiencies found in the experiment [15]. A possible reason for the comparatively low energy efficiency obtained by the model calculations consists in an overestimation of the electron energy loss due to vibrational and/or electronic excitation as a consequence of insufficient cross section data [41]. Furthermore, once a CO_2 molecule is electronically excited, it often dissociates into neutral fragments like CO and O, but the knowledge about these processes leading to an increase of CO and O is improvable as well. When assuming that both the electronically excited states CO_2^* and CO_2^{**} undergo a very rapid dissociation to give a CO molecule and an O atom [68], an energy efficiency of 7.6 % is obtained by the present model calculations for the standard condition. When following Pietanza *et al.* [69] and supposing that only the electronically excited state CO_2^* contributes directly to the CO_2 dissociation, energy efficiencies

η in the range between 4 and 5 % are predicted by the present model calculations for the parameter conditions of table 6. These values are in good agreement with the energy efficiencies of $\eta < 5\,\%$ measured in [15]. They are also in conformity with the value obtained by global modelling in [16]. However, the electronically excited state CO_2^* is not mentioned to contribute to the dissociation in that paper. Note that the change of the reaction E38 in table 2 into a direct dissociation process does not affect the discharge characteristics except for the densities of CO and O.

In order to compare the present modelling results directly with the measured CO_2 conversion degree and specific energy input from Brehmer *et al.* [15] for the same discharge conditions as used here, the parameters α and SEI are determined according to

$$\alpha = \frac{\Delta n_{CO}}{n_{CO_2}} \frac{t_r}{T} \tag{22}$$

$$\mathrm{SEI} = \frac{P_d}{n_{CO_2}} t_r \tag{23}$$

for the measured residence times t_r of 70, 230 and 800 ms [15], respectively. Figure 10 shows that the scaling of the modelling results with the experimental residence times leads to a fair agreement of the specific energy input from the experiment and the SEI predicted by the model. From this

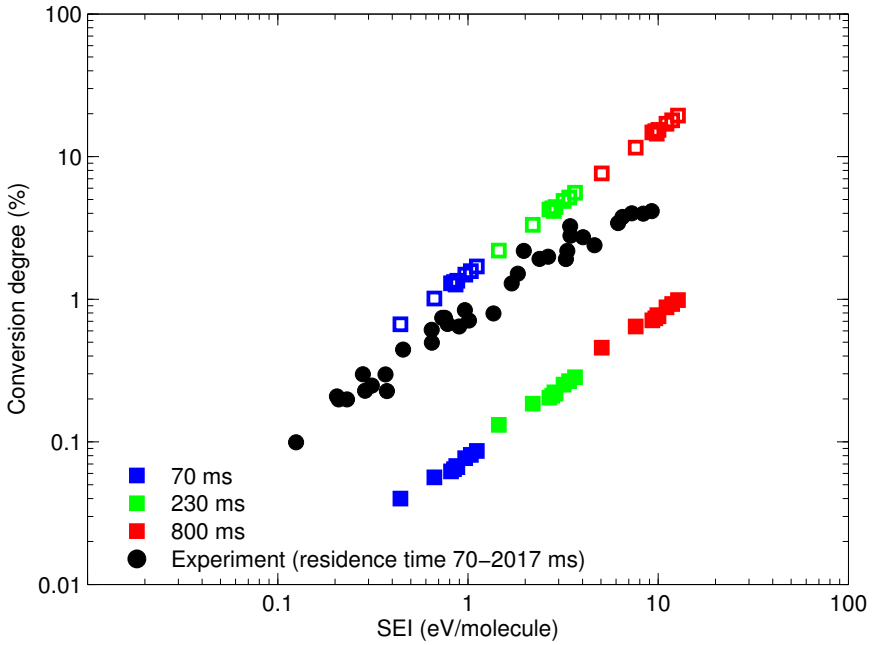

Figure 10: Calculated CO_2 conversion degree as a function of the specific energy input for residence times of 70, 230 and 800 ms in comparison with the measured data of Brehmer *et al.* [15] for a dielectric barrier thicknesses of 2 mm without (full symbols) and with (open symbols) the contribution of CO_2^* to the CO_2 dissociation according to Pietanza *et al.* [69].

fact it can be concluded that the considered self-consistent time- and space-dependent fluid model provides a good prediction of the electrical characteristics of the discharge.

Furthermore, figure 10 shows that the slope of the increase of the conversion degree with increasing SEI is well predicted by the present model while the conversion degree α is underestimated by one order of magnitude if the contribution of CO_2^* to the CO_2 dissociation according to Pietanza *et al.* [69] is not taken into account. Inclusion of the latter leads to a slight overestimation of the conversion degree for a given SEI by roughly a factor of two. That is, further work is needed in

order to clarify the role of the different reaction channels contributing to the CO_2 dissociation. For example, further additional processes not included in the present reaction kinetics model could also lead to the production of CO. Here, especially CO_2 reactions with various ions are to mention which were found to contribute to 60 % to the dissociation of CO_2 in the atmospheric pressure DBD with a frequency of 35 kHz and power density of 10.6 W cm^{-3} studied by a global time-dependent model in [16]. This global modelling was done for residence times between 0.5 and 5 s. However, these processes are negligible for the discharge conditions and period of time considered in the present time- and space-dependent fluid modelling. This finding is in accordance with [33], where up to five pulses in an atmospheric pressure DBD with a frequency of 50 kHz and a power of 150 W were analysed by a global model including an extensive plasma chemistry model and electron impact reactions were found to dominate the splitting of CO_2. Moreover, more recent global modelling studies of CO_2 dielectric barrier discharges reported in [17] also show the predominance of the electron impact reactions for the dissociation of CO_2. The extension of the present fluid model to take CO_2 reactions with various ions and further processes into account to clarify the influence of heavy particle collisions on the CO production will be subject of future studies.

The description of the CO_2 conversion degree in terms of the universal scaling parameter SEI becomes possible because most of the energy is injected into the DBD plasma during the formation of the filaments and is dissipated almost immediately due to different electron collision processes for the most part according to the fractional power shown in figure 2. This situation takes place in the case of CO_2 dissociation, i.e. net CO production, at the cold conditions used in a typical DBD in pure CO_2, because the CO produced is very stable and cannot be easily oxidized or reduced so that loss processes of CO are slow. For example, one of the expected loss reactions is the recombination of CO and O back to CO_2. This reaction is spin forbidden [70] and occurs only very slowly in the gas phase (reactions N2 and N3 in table 5) or on non-catalytic surfaces like quartz. The loss of CO due to electron impact dissociation is negligible because it requires about twice as much energy than the electron impact dissociation of CO_2 and the electron impact ionization of CO was found to be less important for conversion degrees less than 15 % [17].

As an extension, it can be expected that a description of an electron induced production process in terms of the specific energy input is fairly general independent of the gas mixture. That is, if the fractional power transferred is the determining variable, the density of a chemical species produced by an electron impact collision process with ground state molecules should scale only with the specific energy input in a filamentary dielectric barrier discharge. One example is the ozone generation in dielectric barrier discharges [71, 72]. However, here the ozone yield scales with the specific energy input only over a limited parameter range because of the thermal destruction of ozone at elevated temperatures [72].

4 Summary

The conversion of CO_2 into CO and by-products was investigated by means of a self-consistent fluid modelling approach. Model calculations were performed for a wide range of discharge conditions related to the DBD reactor used by Brehmer *et al.* [15]. The analysis of the discharge behaviour and the general features of CO production can be summarized as follows.

For the standard condition, comprising a voltage amplitude of 10 kV at a frequency of 130 kHz, a gas pressure of 1 bar at a gas temperature of 400 K and a gap width of 1 mm with 2 mm thick quartz dielectrics on both sides, differences in the discharge evolution in positive and negative voltage half-cycles appear. It was found that discharges occurring in negative half-cycles of the applied voltage are characterized by a higher breakdown voltage, stronger current peaks and longer period with

higher electron density compared to discharges in positive half-cycles. The differences between positive and negative half-cycles were ascribed to the occurrence of volume memory effects which lead to a mutual influencing of sequent discharge events. In particular, the high inertia of negative ions compared to the electron component and the relatively high frequency result in a predominance of CO_3^- in positive half-cycles while electrons constitute the dominant negatively charged species in negative half-cycles. It was also shown that the different properties of the individual discharge events in positive and negative half-cycles lead to a spatially asymmetric distribution of the stable neutrals like CO molecules and O atoms in the gap.

The exploration of the CO_2 dissociation mechanisms revealed that for the present discharge conditions the electron impact dissociation is the dominant CO production channel (contribution of about 80 % to the total dissociation) while dissociative electron attachment and recombination processes contribute only weakly to the CO_2 dissociation (contribution of about 10 % from each). The analysis of the spatiotemporal change of the different dissociation channels showed that the electron impact dissociation has its maxima at the sheath edges as a result of the spatial distribution of the electron density and the mean electron energy at the instants of maximum current while the rate of dissociative electron attachment is almost equally distributed over the gap. The dissociative recombination processes occur exclusively in the quasi-neutral plasma region. Furthermore, the CO production in heavy particle collision processes and due to vibrational up-pumping along the asymmetric stretch was found to be negligible in the gas temperature range considered.

The total CO production rate was found to be largest for a short duration of a few nanoseconds during breakdown as a consequence of the dramatic increase of the electron density with ignition of the individual discharge events. This leads to a step-wise increase of the line integrated CO density in the gap of about $1.5 \times 10^{11}\,\mathrm{cm}^{-2}$ during each discharge pulse.

Besides the standard condition, model calculations for different pressures, gas temperatures, voltage amplitudes, frequencies and permittivities of the dielectrics were performed. Here, one parameter was changed for the respective parameter variation while keeping the other parameters constant. A different power density coupled into the plasma and a different CO_2 conversion frequency were obtained for each parameter set. In accordance with the experimental results of Brehmer *et al.* [15] it was found that the CO_2 conversion frequency depends linearly on the power spent per CO_2 molecule but it does not depend directly on any of the investigated input parameters.

In order to compare the CO production predicted by the fluid model directly with measured conversion degrees in dependence on the specific energy input, the respective properties obtained for the different discharge conditions were scaled by the experimental residence times of a gas volume in the active plasma zone. From this approach, a fairly good agreement of the measured SEI and the SEI predicted by the model was obtained. In addition, the slope of the linear increase of the conversion degree with increasing SEI in log-log scale obtained from the modelling results for the different parameter sets does coincide with that reported in [15] to a large extend.

However, the conversion degree obtained from the present model for a given SEI and thus the energy efficiency of CO production turned out to be smaller than the experimental values by about one order of magnitude. As a possible reason for this drawback the immediate dissociation of the electronically excited states CO_2^* and CO_2^{**} as additional CO_2 conversion channels according to [68, 69] were discussed and tested. It was also verified that the change of the excitation reactions into direct dissociation channels does not have any influence on other discharge properies than the densities of the dissociation products CO and O.

A strong overestimation of the energy efficiency was obtained when assuming that both the electronically excited states undergo a very rapid dissociation to give a CO molecule and an O atom. When following Pietanza *et al.* [69] and supposing that only the electronically excited state

CO_2^* contributes directly to the CO_2 dissociation, energy efficiencies in the range of $\eta = 4 \ldots 5\,\%$ are predicted for the considered data range. These values are in the same order of magnitude as the energy efficiencies of $\eta = 1.5 \ldots 3.5\,\%$ obtained experimentally by Brehmer *et al.* [15] and also coincide roughly with the results of a global reaction kinetics model in [16] which does not include the direct dissociation of CO_2^* as a CO production channel. In that paper other processes occurring mainly at higher dissociation degrees are mentioned to contribute markedly to the CO production. The extension of the present fluid model to take CO_2 reactions with various ions and further processes into account to clarify the influence of heavy particle collisions at higher dissociation degrees on the CO production will be subject of future studies.

Acknowledgment

The work was partly supported by the German research foundation within the Collaborative Research Centre Transregio 24 and under grant LO 623/3-1. SP and RE would like to express gratitude to Dr. A. Bol and Prof. Dr. Ir. W. M. M. Kessels of PMP group at Eindhoven University of Technology for making available the computational resources. Authors thank Dr. F. Brehmer for providing the experimental data represented in figure 10.

References

[1] A. Lebouvier, S. A. Iwarere, P. d'Argenlieu, D. Ramjugernath, and L. Fulcheri. Assessment of Carbon Dioxide Dissociation as a New Route for Syngas Production: A Comparative Review and Potential of Plasma-Based Technologies. *Energy Fuels*, 27(5):2712–2722, 2013.

[2] C.-J. Liu, G.-H. Xu, and T. Wang. Non-thermal plasma approaches in CO_2 utilization. *Fuel Process. Technol.*, 58(2-3):119–134, 1999.

[3] L. C. Brown and A. T. Bell. Kinetics of the Oxidation of Carbon Monoxide and the Decomposition of Carbon Dioxide in a Radiofrequency Electric Discharge. I. Experimental Results. *Ind. Eng. Chem. Fundam.*, 13(3):203–210, 1974.

[4] V. D. Rusanov, A. A. Fridman, and G. V. Sholin. The physics of a chemically active plasma with nonequilibrium vibrational excitation of molecules. *Sov. Phys. Usp.*, 24(6):447–474, 1981.

[5] A. A. Fridman and V. D. Rusanov. Theoretical basis of non-equilibrium near atmospheric pressure plasma chemistry. *Pure Appl. Chem.*, 66(6):1267–1278, 1994.

[6] A. A. Fridman. *Plasma Chemistry*. Cambridge University Press, 2008.

[7] A. Yamamoto, S. Mori, and M. Suzuki. Scale-up or numbering-up of a micro plasma reactor for the carbon dioxide decomposition. *Thin Solid Films*, 515(9):4296–4300, 2007. {SPSM} 18 - The 18th Symposium on Plasma Science for MaterialsSPSM 18.

[8] L. F. Spencer and A. D. Gallimore. Efficiency of CO_2 Dissociation in a Radio-Frequency Discharge. *Plasma Chem. Plasma Process.*, 31(1):79–89, 2011.

[9] T. Nunnally, K. Gutsol, A. Rabinovich, A. Fridman, A. Gutsol, and A. Kemoun. Dissociation of CO_2 in a low current gliding arc plasmatron. *J. Phys. D: Appl. Phys.*, 44(27):274009, 2011.

[10] L. F. Spencer and A. D. Gallimore. CO_2 dissociation in an atmospheric pressure plasma/catalyst system: a study of efficiency. *Plasma Sources Sci. Technol.*, 22(1):015019, 2013.

[11] R. Li, Q. Tang, S. Yin, and T. Sato. Plasma catalysis for CO_2 decomposition by using different dielectric materials . *Fuel Process. Technol.*, 87(7):617–622, 2006.

[12] S. Paulussen, B. Verheyde, X. Tu, C. De Bie, T. Martens, D. Petrovic, A. Bogaerts, and B. Sels. Conversion of carbon dioxide to value-added chemicals in atmospheric pressure dielectric barrier discharges. *Plasma Sources Sci. Technol.*, 19(3):034015, 2010.

[13] Q. Yu, M. Kong, T. Liu, J. Fei, and X. Zheng. Characteristics of the Decomposition of CO_2 in a Dielectric Packed-Bed Plasma Reactor. *Plasma Chem. Plasma Process.*, 32(1):153–163, 2012.

[14] S. Wang, Y. Zhang, X. Liu, and X. Wang. Enhancement of CO_2 Conversion Rate and Conversion Efficiency by Homogeneous Discharges. *Plasma Chem. Plasma Process.*, 32(5):979–989, 2012.

[15] F. Brehmer, S. Welzel, M. C. M. van de Sanden, and R. Engeln. CO and byproduct formation during CO_2 reduction in dielectric barrier discharges. *J. Appl. Phys.*, 116(12):123303, 2014.

[16] T. Kozák and A. Bogaerts. Splitting of CO_2 by vibrational excitation in non-equilibrium plasmas: a reaction kinetics model. *Plasma Sources Sci. Technol.*, 23(4):045004, 2014.

[17] R. Aerts, W. Somers, and A. Bogaerts. Carbon Dioxide Splitting in a Dielectric Barrier Discharge Plasma: A Combined Experimental and Computational Study. *ChemSusChem*, 8(4):702–716, 2015.

[18] X. Duan, Y. Li, W. Ge, and B. Wang. Degradation of co_2 through dielectric barrier discharge microplasma. *Greenhouse Gas. Sci. Technol.*, 5(2):131–140, 2015.

[19] D. Mei, X. Zhu, Y.-L. He, J. D. Yan, and X. Tu. Plasma-assisted conversion of CO_2 in a dielectric barrier discharge reactor: understanding the effect of packing materials. *Plasma Sources Science and Technology*, 24(1):015011, 2015.

[20] D. Loffhagen and F. Sigeneger. Advances in Boltzmann equation based modelling of discharge plasmas. *Plasma Sources Sci. Technol.*, 18(3):034006, 2009.

[21] L. C. Brown and A. T. Bell. Kinetics of the Oxidation of Carbon Monoxide and the Decomposition of Carbon Dioxide in a Radiofrequency Electric Discharge. II. Theoretical Interpretation. *Ind. Eng. Chem. Fundam.*, 13(3):210–218, 1974.

[22] A. Cenian, A. Chernukho, V. Borodin, and G. Śliwiński. Modeling of Plasma-Chemical Reactions in Gas Mixture of CO_2 Lasers I. Gas Decomposition in Pure CO_2 Glow Discharge. *Contrib. Plasma Phys.*, 34(1):25–37, 1994.

[23] T. Kozák and A. Bogaerts. Evaluation of the energy efficiency of CO_2 conversion in microwave discharges using a reaction kinetics model. *Plasma Sources Sci. Technol.*, 24(1):015024, 2015.

[24] W. J. Wiegand and W. L. Nighan. Plasma chemistry of CO_2-N_2-He discharges. *Appl. Phys. Lett.*, 22(11):583–586, 1973.

[25] H. Hokazono and H. Fujimoto. Theoretical analysis of the CO_2 molecule decomposition and contaminants yield in transversely excited atmospheric CO_2 laser discharge. *J. Appl. Phys.*, 62(5):1585–1594, 1987.

[26] H. Hokazono and M. Obara. Reduction of the CO_2 decomposition in the transversely excited atmospheric CO_2 laser discharge plasma by a very small amount of the water vapor. *Appl. Phys. Lett.*, 57(1):4–6, 1990.

[27] H. Hokazono, N. Kobayashi, and M. Obara. Catalytic control requirements for the stable operation of the closed-cycle, transversely excited atmospheric co$_2$ laser. *J. Appl. Phys.*, 70(4):1962–1965, 1991.

[28] H. Hokazono, M. Obara, K. Midorikawa, and H. Tashiro. Theoretical operational life study of the closed-cycle transversely excited atmospheric CO_2 laser. *J. Appl. Phys.*, 69(10):6850–6868, 1991.

[29] S. R. Byron and H. Apter. Model of gas composition and plasma properties in sealed cw CO_2 lasers. *J. Appl. Phys.*, 71(4):1976–1991, 1992.

[30] A. Cenian, A. Chernukho, and V. Borodin. Modeling of Plasma-Chemical Reactions in Gas Mixture of CO_2 lasers. II. Theoretical Model and its Verification. *Contrib. Plasma Phys.*, 35(3):273–296, 1995.

[31] A. Cenian, A. Chernukho, P. Kukiello, R. Zaremba, V. Borodin, and G. Sliwinski. Improvement of self-regeneration of gas mixtures in a c onvection-cooled 1.2 kW CO_2 laser. *J. Phys. D: Appl. Phys.*, 30(7):1103–1110, 1997.

[32] B. Eliasson, W. Egli, and U. Kogelschatz. Modelling of dielectric barrier discharge chemistry. *Pure Appl. Chem.*, 66(6):1275–1286, 1994.

[33] R. Aerts, T. Martens, and A. Bogaerts. Influence of Vibrational States on CO_2 Splitting by Dielectric Barrier Discharges. *J. Phys. Chem. C*, 116(44):23257–23273, 2012.

[34] R. Aerts, T. Martens, and A. Bogaerts. Correction to "Influence of Vibrational States on CO_2 Splitting by Dielectric Barrier Discharge". *J. Phys. Chem. C*, 118(48):28330–28330, 2014.

[35] A. von Keudell and J. Benedikt. A Physicist's Perspective on "Views on Macroscopic Kinetics of Plasma Polymerisation". *Plasma Process. Polym.*, 7(5):376–379, 2010.

[36] M. M. Becker, T. Hoder, R. Brandenburg, and D. Loffhagen. Analysis of microdischarges in asymmetric dielectric barrier discharges in argon. *J. Phys. D: Appl. Phys.*, 46(35):355203, 2013.

[37] H. Höft, M. Kettlitz, M. M. Becker, T. Hoder, D. Loffhagen, R. Brandenburg, and K.-D. Weltmann. Breakdown characteristics in pulsed-driven dielectric barrier discharges: influence of the pre-breakdown phase due to volume memory effects. *J. Phys. D: Appl. Phys.*, 47(46):465206, 2014.

[38] R. Winkler and M. W. Wuttke. A detailed study of electron kinetics involved in modelling discharge pumped excimer laser plasmas. *Appl. Phys. B*, 54(1):1–17, 1992.

[39] M. Gnybida, D. Loffhagen, and D. Uhrlandt. Fluid Modeling and Analysis of the Constriction of the DC Positive Column in Argon. *IEEE Trans. Plasma Sci.*, 37(7):1208–1218, July 2009.

[40] V. N. Ochkin. *Spectroscopy of low temperature plasma.* John Wiley and Sons, 2009.

[41] Y. Itikawa. Cross sections for electron collisions with carbon dioxide. *J. Phys. Chem. Ref. Data*, 31(3):749–767, 2002.

[42] A. V. Phelps. Compilation of electron cross sections used by A. V. Phelps. http://jilawww.colorado.edu/∼avp/collision_data/electronneutral/ELECTRON.TXT.

[43] S. Biagi. Cross sections used by Magboltz 7.1. http://rjd.web.cern.ch/rjd/cgi-bin/cross?update.

[44] M. Allan. Vibrational structures in electron-CO_2 scattering below the $^2\Pi_u$ shape resonance. *J. Phys. B: At. Mol. Opt. Phys.*, 35(17):L387–L395, 2002.

[45] B. Peart, R. Forrest, and K. T. Dolder. Measurements of cross sections for detachment of electrons from C^- and O^- ions by electron impact. *J. Phys. B: Atom. Molec. Phys.*, 12(5):847–853, 1979.

[46] B. Peart, R. A. Forrest, and K. Dolder. A search for structure in cross sections for detachment from C^- and O^- ions by electron impact. *J. Phys. B: Atom. Molec. Phys.*, 12(16):2735–2739, 1979.

[47] D. Rapp and D. D. Briglia. Total Cross Sections for Ionization and Attachment in Gases by Electron Impact. II. Negative-Ion Formation. *J. Chem. Phys.*, 43(5):1480–1489, 1965.

[48] A. A. Viggiano, A. Ehlerding, F. Hellberg, R. D. Thomas, V. Zhaunerchyk, W. D. Geppert, H. Montaigne, M. Larsson, M. Kaminska, and F. Österdahl. Rate constants and branching ratios for the dissociative recombination of CO_2^+. *J. Chem. Phys*, 122(22):226101, 2005.

[49] R. E. Beverly III. Ion aging effects on the dissociative-attachment instability in CO_2 lasers. *Opt. Quant. Electron.*, 14(6):501–513, 1982.

[50] J. T. Gudmundsson and E. G. Thorsteinsson. Oxygen discharges diluted with argon: dissociation processes. *Plasma Sources Sci. Technol.*, 16(2):399–412, 2007.

[51] J. A. Blauer and G. R. Nickerson. A survey of vibrational relaxation rate data for processes important to CO_2-N_2-H_2O infrared plume radiation. Technical Report AFRPL-TR-73-57, Air Force Rocket Propulsion Laboratory, Edwards, California 93523, 1973.

[52] K. Smith and R. M. Thomson. *Computer Modeling of Gas Lasers.* Plenum Press, New York, 1978.

[53] W. Tsang and R. F. Hampson. Chemical Kinetic Data Base for Combustion Chemistry. Part I. Methane and Related Compounds. *J. Phys. Chem. Ref. Data*, 15(3):1087–1279, 1986.

[54] D. L. Baulch, R. A. Cox, P. J. Crutzen, R. F. Hampson, J. A. Kerr, J. Troe, and R. T. Watson. Evaluated Kinetic and Photochemical Data for Atmospheric Chemistry: Supplement I CODATA Task Group on Chemical Kinetics. *J. Phys. Chem. Ref. Data*, 11(2):327–496, 1982.

[55] E. W. Schlag, R. Frey, B. Gotchev, W. B. Peatman, and H. Pollak. Radiative lifetimes of ions from electron-photon coincidence measurements. *Chem. Phys. Lett.*, 51(3):406–408, 1977.

[56] L. A. Viehland and E. A. Mason. Transport Properties of Gaseous Ions over a Wide Energy Range, IV. *At. Data Nucl. Data Tables*, 60(1):37–95, 1995.

[57] H. W. Ellis, R. Y. Pai, E. W. McDaniel, E. A. Mason, and L. A. Viehland. Transport properties of gaseous ions over a wide energy range. *At. Data Nucl. Data Tables*, 17(3):177–210, 1976.

[58] G. Ember, J. R. Ferron, and K. Wohl. Self-Diffusion Coefficients of Carbon Dioxide at 1180°–1680°K. *J. Chem. Phys.*, 37(4):891–897, 1962.

[59] T. R. Marrero and E. A. Mason. Gaseous Diffusion Coefficients. *J. Phys. Chem. Ref. Data*, 1(1):3–118, 1972.

[60] G. K. Grubert, M. M. Becker, and D. Loffhagen. Why the local-mean-energy approximation should be used in hydrodynamic plasma descriptions instead of the local-field approximation. *Phys. Rev. E*, 80:036405, 2009.

[61] H. Leyh, D. Loffhagen, and R. Winkler. A new multi-term solution technique for the electron Boltzmann equation of weakly ionized steady-state plasmas. *Comput. Phys. Commun.*, 113(1):33–48, 1998.

[62] G. J. M. Hagelaar and L. C. Pitchford. Solving the Boltzmann equation to obtain electron transport coefficients and rate coefficients for fluid models. *Plasma Sources Sci. Technol.*, 14(4):722, 2005.

[63] M. Capitelli, G. Colonna, G. D'Ammando, V. Laporta, and A. Laricchiuta. Nonequilibrium dissociation mechanisms in low temperature nitrogen and carbon monoxide plasmas. *Chem. Phys.*, 438:31–36, 2014.

[64] D. Braun, V. Gibalov, and G. Pietsch. Two-dimensional modelling of the dielectric barrier discharge in air. *Plasma Sources Sci. Technol.*, 1(3):166–174, 1992.

[65] M. M. Becker, D. Loffhagen, and W. Schmidt. A stabilized finite element method for modeling of gas discharges. *Comput. Phys. Commun.*, 180(8):1230–1241, 2009.

[66] Yu. B. Golubovskii, V. A. Maiorov, J. Behnke, and J. F. Behnke. Modelling of the homogeneous barrier discharge in helium at atmospheric pressure. *J. Phys. D: Appl. Phys.*, 36:39–49, 2003.

[67] P. S. Gardiner, J. L. Moruzzi, and J. D. Craggs. Negative ions in Trichel corona in carbon dioxide and oxygen. *J. Phys. D: Appl. Phys.*, 11(3):237, 1978.

[68] C. Willis, W. J. Sarjeant, and D. M. Wardlaw. Initial rate of decomposition of CO_2 in volume discharges: An experimental study. *J. Appl. Phys.*, 50(1):68–72, 1979.

[69] L. D. Pietanza, G. Colonna, G. D'Ammando, A. Laricchiuta, and M. Capitelli. Vibrational excitation and dissociation mechanisms of CO_2 under non-equilibrium discharge and post-discharge conditions. *Plasma Sources Sci. Technol.*, 24(4):042002, 2015.

[70] D.-Y. Hwang and A. M. Mebel. Ab initio study of spin-forbidden unimolecular decomposition of carbon dioxide. *Chem. Phys.*, 256(2):169–176, 2000.

[71] N. Mericam-Bourdet, M. J. Kirkpatrick, F. Tuvache, D. Frochot, and E. Odic. Effect of voltage waveform on dielectric barrier discharge ozone production efficiency. *Eur. Phys. J. Appl. Phys.*, 57:30801, 3 2012.

[72] B. Eliasson, M. Hirth, and U. Kogelschatz. Ozone synthesis from oxygen in dielectric barrier discharges. *J. Phys. D: Appl. Phys.*, 20:1421–1437, 1987.